A multiwavelength view of the galaxy cluster Abell 523 and its peculiar diffuse radio source

M. Girardi,[1,2]★ W. Boschin,[3,4,5] F. Gastaldello,[6,7] G. Giovannini,[8,9] F. Govoni,[10] M. Murgia,[10] R. Barrena,[4,5] S. Ettori,[11,12] M. Trasatti[8,9] and V. Vacca[10,13]

[1]*Dipartimento di Fisica, Università degli Studi di Trieste, via Tiepolo 11, I-34143 Trieste, Italy*
[2]*INAF-Osservatorio Astronomico di Trieste, via Tiepolo 11, I-34143 Trieste, Italy*
[3]*Fundación G. Galilei - INAF (Telescopio Nazionale Galileo), Rambla J. A. Fernández Pérez 7, E-38712 Breña Baja (La Palma), Spain*
[4]*Instituto de Astrofísica de Canarias, C/Vía Láctea s/n, E-38205 La Laguna (Tenerife), Spain*
[5]*Departamento de Astrofísica, Univ. de La Laguna, Av. del Astrofísico Francisco Sánchez s/n, E-38205 La Laguna (Tenerife), Spain*
[6]*INAF-IASF Milano, Via Bassini 15, I-20133 Milano, Italy*
[7]*Department of Physics and Astronomy, University of California at Irvine, 4129 Frederick Reines Hall, Irvine, CA 92697-4575, USA*
[8]*Dipartimento di Fisica e Astronomia, Università degli Studi di Bologna, via Ranzani 1, I-40127 Bologna, Italy*
[9]*INAF-Osservatorio di Radioastronomia, via Gobetti 101, I-40129 Bologna, Italy*
[10]*INAF-Osservatorio Astronomico di Cagliari, Via della Scienza 5, I-09047 Selargius, Cagliari, Italy*
[11]*INAF-Osservatorio Astronomico di Bologna, via Ranzani 1, I-40127, Bologna, Italy*
[12]*INFN - Sezione di Bologna, viale Berti Pichat 6/2, I-40127, Bologna, Italy*
[13]*Max Planck Institute for Astrophysics, Karl-Schwarzschild-Str. 1, D-85748 Garching, Germany*

ABSTRACT

We study the structure of the galaxy cluster Abell 523 (A523) at $z = 0.104$ using new spectroscopic data for 132 galaxies acquired at the Telescopio Nazionale *Galileo*, new photometric data from the *Isaac Newton* Telescope, and X-ray and radio data from the *Chandra* and Very Large Array archives. We estimate the velocity dispersion of the galaxy population, $\sigma_V = 949^{+80}_{-60}$ km s^{-1}, and the X-ray temperature of the hot intracluster medium, $kT = 5.3 \pm 0.3$ keV. We infer that A523 is a massive system: $M_{200} \sim 7$–9×10^{14} M$_\odot$. The analysis of the optical data confirms the presence of two subclusters, 0.75 Mpc apart, tracing the SSW-NNE direction and dominated by the two brightest cluster galaxies (BCG1 and BCG2). The X-ray surface brightness is strongly elongated towards the NNE direction, and its peak is clearly offset from both the brightest cluster galaxies (BCGs). We confirm the presence of a 1.3 Mpc large radio halo, elongated in the ESE-WNW direction and perpendicular to the optical/X-ray elongation. We detect a significant radio/X-ray offset and radio polarization, two features which might be the result of a magnetic field energy spread on large spatial scales. A523 is found consistent with most scaling relations followed by clusters hosting radio haloes, but quite peculiar in the P_{radio}–L_X relation: it is underluminous in the X-rays or overluminous in radio. A523 can be described as a binary head-on merger caught after a collision along the SSW-NNE direction. However, minor optical and radio features suggest a more complex cluster structure, with A523 forming at the crossing of two filaments along the SSW-NNE and ESE-WNW directions.

Key words: galaxies: clusters: general – galaxies: clusters: individual: Abell 523 – galaxies: kinematics and dynamics – radio continuum: general – X-rays: galaxies: clusters.

1 INTRODUCTION

Clusters of galaxies are the largest gravitationally bound systems in the Universe, with typical masses of about 10^{14}–10^{15} M$_\odot$.

Clusters are formed by hierarchical formation processes, where smaller units (galaxies, groups and small clusters) formed first and merged under gravitational pull to larger and larger units in the course of time, clusters forming at the intersection of filaments of the large-scale structure of the Universe. Merging processes are the subject of multiwavelength studies (e.g. Feretti, Gioia & Giovannini 2002). Major cluster mergers are among the most

★ E-mail: girardi@oats.inaf.it

energetic events in the Universe since the big bang (e.g. Sarazin 2002).

An increasing number of galaxy clusters shows the presence of diffuse radio emission on Mpc scale (e.g. Feretti 2005; Ferrari et al. 2008; Venturi 2011; Feretti et al. 2012). The synchrotron emission of these radio sources proves the existence of a large-scale magnetic field and relativistic particles spread out in the cluster. These extended diffuse radio sources are usually classified as relics and haloes, having quite different phenomenological properties (e.g. Giovannini & Feretti 2004; Feretti et al. 2012). For both types of sources, cluster mergers have been proposed as the process responsible for their origin (e.g. Trimble 1993; Feretti 1999; Brunetti & Jones 2015). This scenario is supported by an increasing amount of observational evidence (e.g. Schuecker et al. 2001; Buote 2002; Cassano et al. 2010; Rossetti et al. 2011; Girardi et al. 2011 and references therein).

Relics are elongated sources, found at the cluster outskirts, with the major axis roughly perpendicular to the direction of the cluster merger (e.g. van van Weeren et al. 2011b). When observed with high angular resolution, they generally show an asymmetric transverse profile, with a sharp edge usually on the side towards the cluster outer edge. These morphologies are in very good agreement with models predicting that these sources are related to large-scale shocks generated during cluster merger events (e.g. Enßlin et al. 1998; Brüggen, van Weeren & Röttgering 2011). Instead, radio haloes have rounder morphologies, are unpolarized and fill the central cluster regions occupied by the X-ray emitting intracluster medium (ICM). A close similarity between the radio and the X-ray morphology has been found in a number of clusters hosting a radio halo (e.g. Govoni et al. 2001a). Radio haloes are probably related to turbulent motions of ICM due to merger events (e.g. Brunetti et al. 2009; Brunetti & Jones 2015).

There are also diffuse radio emissions with peculiar properties, e.g. relic sources with a roundish structure (Feretti 2006), the relic of 1RXS J0603.3+4214 with an unusual morphology (Ogrean et al. 2013), haloes having offsets between the radio and the X-ray peak (Govoni et al. 2012). In addition, examples of bridges between relics and haloes have been observed in a few clusters (e.g. Coma cluster – Kim et al. 1989; Abell 2744 – Govoni et al. 2001a), and diffuse radio sources at large distances from a few clusters have been detected (e.g. Abell 2255 – Pizzo et al. 2008; Abell 2256 – van Weeren et al. 2009). An intriguing case is also that of the diffuse source 0809+39 (Brown & Rudnick 2009), where the southern component is possibly associated with an $\sim$5 Mpc long galaxy filament at $z \sim 0.04$.

The present paper is focused on the study of Abell 523 (hereafter A523). A523 hosts an extended and powerful diffuse emission with a maximum linear size of $\sim 1.3\, h_{70}^{-1}$ Mpc and a total radio power of $P_{1.4\,\mathrm{GHz}} \sim 1.5\,10^{24}$ W Hz^{-1}, strongly elongated along the ESE-WNW direction (Giovannini et al. 2011, hereafter G11). G11 classified this radio source as a radio halo because of (i) the radio emission permeates both the merging clumps and (ii) the elongated structure does not show any morphological feature typical of radio relics such as high brightness filamentary structures or a transverse flux asymmetry (see e.g. van Weeren et al. 2011a).

However, the A523 radio halo phenomenology is far from the typical one. In fact, (i) the radio halo is strongly elongated in the direction perpendicular to the likely merging axis (see fig. 3 of G11 and our Fig. 1), while, generally, the opposite phenomenology is observed, with the radio halo being elongated in the same direction as the merger (e.g. Abell 520 – Govoni et al. 2001b; Girardi et al. 2008; Abell 2255 – Govoni et al. 2005; Abell 665 – Giovannini & Feretti

2000). More quantitatively, (ii) A523 is peculiar in its deviation from the typical P_{radio}–L_{X} relation having a higher radio power or a lower X-ray luminosity than expected given the estimate of the X-ray luminosity from *ROSAT* data ($L_{\mathrm{X},0.1-2.4\,\mathrm{keV}} \sim 1 \times 10^{44}$ erg s^{-1}; Ebeling et al. 1998; Böhringer et al. 2000).

On the basis of data available at that time, G11 analysed the internal structure of A523. The analysis of a colour selected photometric catalogue of galaxies extracted from the SuperCOSMOS Sky Surveys showed that the cluster is bimodal and elongated along the SSW-NNE direction. The analysis of *ROSAT* X-ray data revealed a bimodal distribution of the hot ICM, with a clear shift between the galaxies and gas distribution, thus suggesting an ongoing merger (see fig. 5 of G11). Unfortunately, so far, only the redshift of the brightest cluster galaxy (hereafter BCG1) has been available and the kinematical analysis based on member galaxies has never been performed.

A523 was included in our observational program aimed to study the internal dynamics of clusters with diffuse radio emission (DARC – Dynamical Analysis of Radio Clusters; see Girardi et al. 2011 and references therein[1]). We obtained new photometric and spectroscopic data acquired at the *Isaac Newton* Telescope (INT) and at the Telescopio Nazionale *Galileo* (TNG). We also analysed very recent, never analysed before, X-ray data from the *Chandra* archive and radio data from the Jansky Very Large Array (VLA) archive data.

This paper is organized as follows. We describe optical observations and present our spectroscopic data catalogue in Section 2, while Section 3 presents our analysis and results based on optical galaxy data. In Sections 4 and 5 we present our analyses and results from X-ray and radio data, respectively. Section 6 is devoted to the interpretation and discussion of the A523 structure based on multiwavelength data.

Throughout this paper, we use $H_0 = 70$ km s^{-1} Mpc^{-1} and $h_{70} = H_0/(70$ km s^{-1} Mpc$^{-1})$ in a flat cosmology with $\Omega_0 = 0.3$ and $\Omega_\Lambda = 0.7$. In the adopted cosmology, 1 arcmin corresponds to $\sim$115 h_{70}^{-1} kpc at the cluster redshift. Unless otherwise stated, we indicate errors at the 68 per cent confidence level (hereafter c.l.).

2 OPTICAL OBSERVATIONS AND DATA SAMPLE

2.1 Spectroscopic and photometric observations

Multi-object spectroscopic observations of A523 were carried out at the TNG in 2012 December and 2014 January. We used the instrument DOLORES in MOS mode with the LR-B Grism.[2] In summary, we observed six MOS masks for a total of 210 slits. The total exposure time was 3600 s for three masks, 5400 s for two masks and 7200 s for the last one.

Reduction of spectra and radial velocities computation with the cross-correlation technique (Tonry & Davis 1979) were performed using standard IRAF[3] tasks, as done with other clusters included in our DARC sample (e.g. Boschin et al. 2012). In two cases (IDs. 65 and 110; see Table 1) the redshift was estimated measuring the

---

[1] See also http://adlibitum.oat.ts.astro.it/girardi/darc, the web site of the DARC project.

[2] http://www.tng.iac.es/instruments/lrs

[3] IRAF is distributed by the National Optical Astronomy Observatories, which are operated by the Association of Universities for Research in Astronomy, Inc., under cooperative agreement with the National Science Foundation.
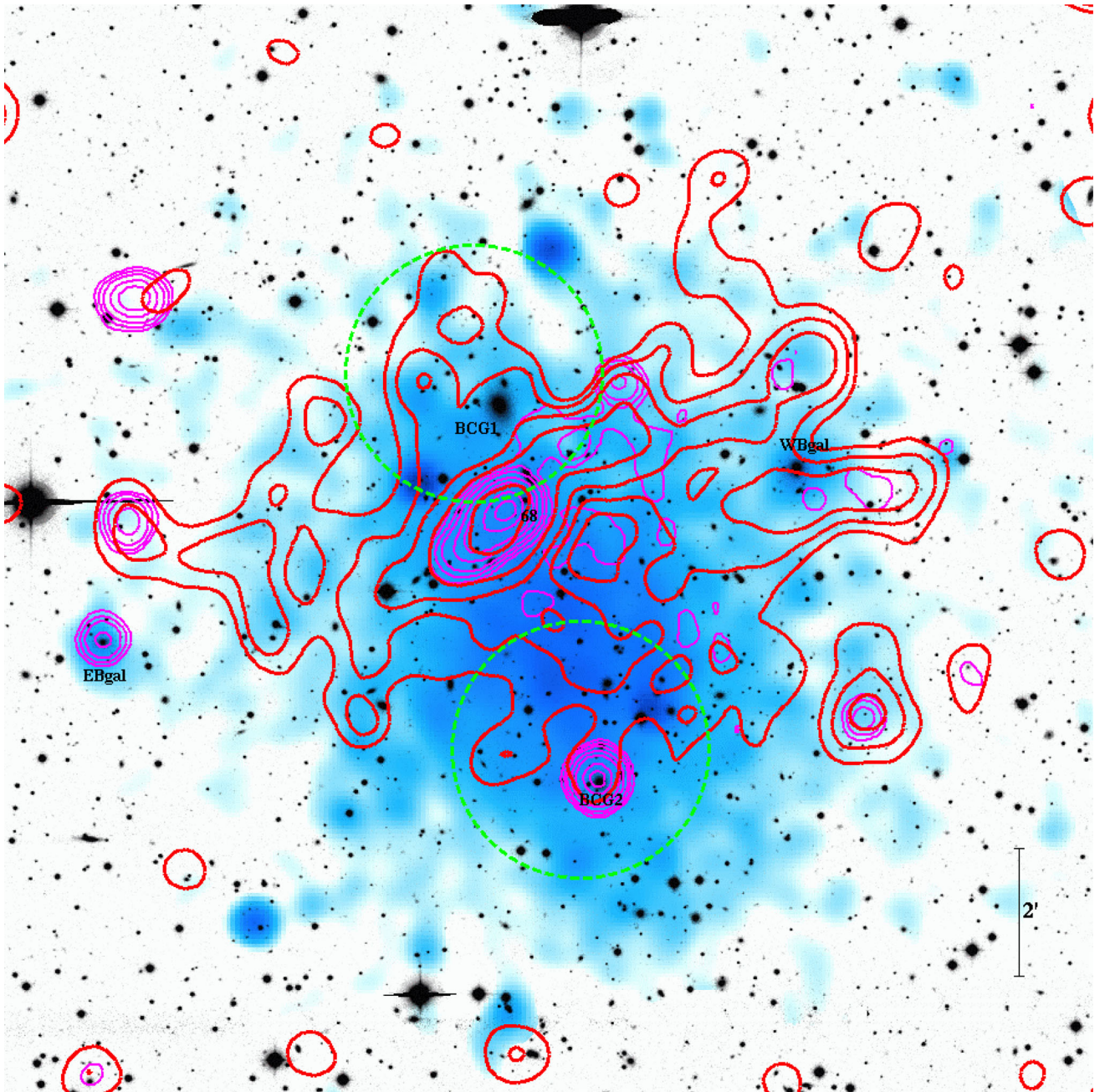
Figure 1. Multiwavelength view of Abell 523. The grey-scale image in background corresponds to the *r* band (INT data). Superimposed, with blue colour, we show the smoothed *Chandra* X-ray image in the 0.5–2 keV energy range (see Section 4). Thin magenta contours refer to the high-resolution 1.4 GHz VLA image and highlight the discrete radio sources. Thick red contours refer to the low-resolution 1.4 GHz VLA image (with discrete sources subtracted) and highlight the radio halo (see Section 5). Dashed green circles indicate the centres of the two subclusters detected through the 2D-DEDICA analysis applied to the photometric member galaxies (see Section 2). Labels refer to specific galaxies discussed in the text. North is up and east is left. At the cluster redshift, the scale of 2 arcmin corresponds to ∼0.23 h_{70}^{-1} Mpc and the FOV of the whole image is 2 × 2 h_{70}^{-1} Mpc.

wavelength location of emission lines in the spectra. Our spectroscopic catalogue lists 132 galaxies in the field of A523. We corrected the nominal velocity errors provided by the cross-correlation technique by multiplying them by a factor of 2.2 as derived from multiple measures of the same targets (e.g. Boschin, Girardi & Barrena 2013). Taking into account the above correction, the average value of the *cz* errors is 72 km s^{-1}.

Our photometric observations were carried out with the Wide Field Camera (WFC), mounted at the prime focus of the 2.5-m

INT telescope. We observed A523 in *g*, *r* and *i* Sloan-Gunn filters in photometric conditions and a seeing of ∼1.4 arcsec. The WFC consists of a four-CCD mosaic covering a 33 × 33 arcmin^2 field of view (FOW), with only a 20 per cent marginally vignetted area. We took nine exposures of 600 s in *g* filter, and nine frames more of 360 s exposure in *r* and *i* filters, respectively. So a total of 5400 s in *g* filter, and 3240 s in *r* and *i* bands. Details on observation procedures and data reduction are described in Barrena et al. (2007). As a final step, we corrected the Galactic extinction $A_g = 0.569$, $A_r = 0.386$

Table 1. Radial velocities of 132 galaxies in the field of A523. For each galaxy, the table lists right ascension and declination, α and δ (J2000); INT dereddened r-band magnitude, r; heliocentric radial velocity, V, with error, ΔV. IDs in italics refer to non-member galaxies. Galaxy ID 75 is the BCG1. Galaxy ID 56 is the BCG2.

ID	α, δ (J2000) (4^h, +8°)	r	V (km	ΔV s^{-1})
1	58 47.73, 48 21.5	19.88	135 555	112
2	58 49.93, 47 54.6	18.26	42 401	70
3	58 52.20, 48 42.6	18.14	30 189	51
4	58 52.28, 55 44.5	17.86	32 223	68
5	58 53.38, 49 39.4	19.50	31 578	59
6	58 53.76, 46 54.4	19.07	30 182	84
7	58 54.06, 48 21.5	17.66	41 879	44
8	58 54.23, 48 42.9	15.73	41 863	40
9	58 54.74, 51 37.7	19.46	31 600	73
10	58 54.78, 42 57.2	17.89	29 600	55
11	58 54.97, 52 20.4	19.60	32 078	132
12	58 55.08, 55 44.5	18.99	42 144	73
13	58 55.12, 43 54.2	18.29	32 798	35
14	58 55.31, 50 16.4	17.82	29 935	42
15	58 55.67, 51 08.5	18.40	32 764	46
16	58 56.00, 50 27.2	17.69	31 039	86
17	58 56.53, 49 36.2	17.11	43 442	35
18	58 56.63, 54 33.2	18.46	42 646	145
19	58 57.66, 48 49.7	17.49	31 756	44
20	58 57.70, 41 21.6	18.20	29 470	37
21	58 57.90, 47 01.0	17.61	41 165	46
22	58 57.72, 45 41.8	18.86	63 627	77
23	58 57.76, 53 26.1	18.59	47 438	88
24	58 57.96, 53 06.8	19.31	47 330	194
25	58 58.67, 56 09.2	20.29	10 848	101
26	58 58.91, 50 45.2	19.46	30 398	70
27	58 58.93, 51 36.9	18.49	30 549	59
28	58 59.02, 45 10.2	17.18	23 945	75
29	58 59.29, 43 57.7	18.68	31 526	44
30	58 59.43, 47 47.7	17.90	32 114	35
31	58 59.57, 45 19.6	19.42	31 090	73
32	58 59.77, 44 49.6	18.23	30 736	51
33	59 00.83, 47 09.5	17.94	32 626	42
34	59 00.90, 53 59.2	19.22	51 820	101
35	59 01.15, 51 25.6	18.65	29 595	66
36	59 01.51, 46 45.5	17.66	40 808	53
37	59 01.90, 57 15.7	17.53	20 563	73
38	59 02.12, 44 55.8	16.96	32 114	35
39	59 02.73, 41 46.5	17.88	30 866	44
40	59 02.99, 45 12.7	17.41	32 133	44
41	59 03.28, 48 20.1	19.91	31 782	103
42	59 03.42, 53 12.3	19.26	41 688	119
43	59 03.64, 42 33.8	18.23	31 831	35
44	59 03.94, 56 32.7	19.99	109 090	108
45	59 03.96, 47 15.4	17.74	30 926	36
46	59 04.03, 41 46.7	16.52	30 757	53
47	59 04.87, 45 17.8	18.49	29 903	163
48	59 04.92, 46 56.0	19.22	31 911	53
49	59 05.17, 43 13.5	20.50	31 887	95
50	59 05.46, 52 25.7	18.93	31 665	55
51	59 05.49, 42 41.0	18.28	31 131	33
52	59 05.54, 45 55.1	17.64	30 677	40
53	59 06.12, 45 21.6	16.51	30 894	40
54	59 06.23, 45 11.8	17.46	42 229	62
55	59 06.49, 44 23.5	17.11	31001	40
56	59 06.59, 43 49.2	15.83	31 222	44
57	59 07.37, 48 54.5	18.40	41 700	134

Table 1 *– continued*

ID	α, δ (J2000) (4^h, +8°)	r	V (km	ΔV s^{-1})
58	59 07.43, 49 20.7	19.00	31 071	70
59	59 07.77, 41 05.2	18.25	32 278	33
60	59 07.96, 50 49.5	18.28	31 089	48
61	59 08.04, 50 13.3	18.00	30 776	70
62	59 08.90, 45 43.8	19.32	32 360	103
63	59 08.98, 43 51.1	18.55	31 380	48
64	59 10.98, 51 04.0	19.71	30 561	134
65	59 11.03, 53 27.9	19.76	45 429	100
66	59 11.17, 48 35.7	16.49	28 498	68
67	59 11.18, 52 49.6	16.35	32 901	44
68	59 11.32, 48 12.6	16.78	30 143	40
69	59 11.90, 54 49.1	18.43	60 294	59
70	59 11.95, 44 14.0	18.45	31 502	46
71	59 12.11, 43 04.0	18.99	83 329	57
72	59 12.65, 50 01.9	16.90	29 941	42
73	59 12.86, 46 59.4	19.00	28 631	114
74	59 12.87, 53 32.8	18.23	41 920	57
75	59 12.94, 49 41.1	14.68	31 053	42
76	59 12.99, 49 14.2	17.98	30 890	42
77	59 13.43, 47 15.6	17.28	30 127	51
78	59 13.91, 44 06.3	18.56	42 410	110
79	59 14.12, 50 44.6	18.25	30 403	44
80	59 14.39, 49 44.5	17.26	31 107	64
81	59 14.48, 43 32.3	19.48	50 143	114
82	59 14.49, 47 10.9	18.48	42 176	66
83	59 14.73, 50 27.1	18.12	32 894	42
84	59 14.99, 55 57.6	20.01	59 596	81
85	59 15.09, 51 52.1	18.81	30 076	39
86	59 15.51, 48 02.2	17.40	30 765	40
87	59 16.00, 45 21.2	16.94	33 072	99
88	59 16.18, 51 06.4	18.44	29 114	62
89	59 16.38, 52 00.7	18.07	30 772	33
90	59 16.54, 43 03.2	18.69	108 965	62
91	59 17.16, 52 58.3	19.20	30 488	121
92	59 17.62, 52 09.0	19.68	42 064	77
93	59 18.10, 46 17.8	19.40	30 659	44
94	59 18.16, 46 58.4	17.32	30 767	35
95	59 20.25, 45 01.1	16.03	20 028	29
96	59 20.41, 54 46.8	16.69	31 786	48
97	59 20.54, 43 43.2	19.91	49 204	119
98	59 20.99, 45 14.7	17.55	30 772	57
99	59 21.77, 50 44.0	19.51	32 911	130
100	59 22.56, 52 00.4	19.26	32 790	123
101	59 23.26, 46 14.9	17.27	29 947	37
102	59 23.32, 45 34.2	19.97	29 535	86
103	59 23.32, 49 40.7	19.23	30 121	92
104	59 25.05, 46 42.3	17.61	32 083	59
105	59 26.67, 46 15.1	20.14	41 988	198
106	59 27.19, 46 04.4	17.75	31 814	51
107	59 29.68, 52 37.6	18.12	31 245	95
108	59 30.46, 52 49.9	18.92	60 220	103
109	59 30.60, 53 23.4	18.74	32 014	136
110	59 32.03, 48 31.5	19.00	45 191	100
111	59 32.60, 51 52.6	17.86	32 103	88
112	59 33.12, 46 34.2	17.62	42 361	44
113	59 33.33, 48 58.1	19.21	126 550	128
114	59 33.97, 45 06.5	17.66	42 559	59
115	59 34.46, 50 55.1	17.48	30 722	48
116	59 35.19, 49 24.1	19.49	32 440	92
117	59 36.06, 49 55.2	19.34	41 935	53
118	59 36.06, 50 18.1	19.24	47 985	112
119	59 36.70, 44 06.8	18.28	42 416	90

Table 1 – *continued*

ID	α, δ (J2000) ($4^h, +8°$)	r	V (km	ΔV s^{-1})
120	59 36.84, 46 58.8	19.43	41 824	123
121	59 38.24, 49 08.5	17.79	31 662	44
122	59 38.70, 46 55.7	18.42	41 001	40
123	59 38.79, 46 16.2	18.70	42 861	81
124	59 39.18, 50 49.3	19.78	63 094	106
125	59 40.78, 46 28.8	18.89	41 288	57
126	59 42.75, 45 29.9	17.13	44 699	40
127	59 43.55, 52 54.1	17.26	42 060	31
128	59 43.84, 47 08.5	19.10	60 116	103
129	59 45.06, 45 39.8	18.97	41 287	99
130	59 48.43, 51 06.9	18.29	71 136	134
131	59 48.83, 47 25.4	16.79	31 365	46
132	59 56.68, 51 10.9	-.-	75 506	119

and $A_i = 0.276$ following values listed by NED.[4] We estimated that our photometric sample is complete down to $g = 22.4$ (23.4), $r = 21.4$ (22.7) and $i = 21.2$ (22.4) for signal-to-noise ratio (S/N)=5 (3) within the observed field.

2.2 Spectroscopic catalogue and notable galaxies

Table 1 lists the velocity catalogue (see also Fig. 2): identification number of each galaxy, ID (Col. 1); right ascension and declination, α and δ (J2000, Col. 2); (dereddened) r magnitude (Col. 3); heliocentric radial velocities, $V = cz_\odot$ (Col. 4) with errors, ΔV (Col. 5). With the exception of one galaxy, INT dereddened magnitudes are available.

The cluster galaxy population is dominated by the galaxy ID 75 (BCG1) lying in the northern region. BCG1 also shows an important, diffuse halo slightly elongated towards SSW (see Fig. 3). There is no obvious discrete X-ray/radio source associated with this galaxy. The second brightest galaxy ID 56 (BCG2) lies in the southern region. BCG2 is 1.1 mag fainter than the brightest galaxy (BCG1) and only 0.7–0.8 mag brighter than other luminous cluster galaxies.

G11 detected nine discrete radio sources in the field of A523 (see their fig. 2), two of them having a measured redshift. The prominent head–tail radio galaxy in the central region of the cluster is the member-galaxy ID 68, while in the South a discrete radio source is associated with the cluster member ID 56 (BCG2). Among the discrete radio sources listed by van Weeren et al. (2011b, see their fig. 6), their source A is the head–tail galaxy cited above, source B is a probable background galaxy (by visual inspection of our INT images) and source C is a pointlike source (quasar?) with unknown redshift.

3 ANALYSIS OF THE OPTICAL DATA

3.1 Member selection and global properties

As usual in the analysis of DARC clusters, the selection of cluster members was performed in two steps. First, we run the 1D version of the adaptive-kernel method by Pisani (1993, hereafter 1D-DEDICA) on the 132 galaxies of our spectroscopic catalogue. DEDICA

---

[4] NASA/IPAC Extragalactic Database which is operated by the Jet Propulsion Laboratory, California Institute of Technology, under contract with the National Aeronautics and Space Administration.

is a non-parametric, scale-independent method for density reconstruction. The output of this method gives a list of groups with related statistical significance and their members. The estimate of the (Gaussian) kernel sizes is done through and iterative, optimized procedure. In the case of A523, the 1D-DEDICA method detects the cluster as a peak at $z \sim 0.103$ populated by 80 galaxies considered as fiducial cluster members (in the range $28\,498 \leq V \leq 33\,072$ km s^{-1}; see Fig. 4). The 52 non-members are four foreground and 48 background galaxies, respectively. In particular, a rich, background peak lies at $z \sim 0.140$ with 26 assigned galaxies (hereafter BACKstruct).

In a second step, we combined the spatial and velocity information by running the 'shifting gapper' method based on a gap of 1000 km s^{-1} (Fadda et al. 1996; Girardi et al. 1996). The 'shifting gapper' method rejects galaxies that are too far in velocity from the main body of galaxies within a fixed bin that shifts along the distance from the cluster centre. We considered the standard values of the velocity gap, 1000 km s^{-1} in the cluster rest frame, and of the radial bin, 0.6 h_{70}^{-1} Mpc. The determination of the centre is not obvious in the case of an unrelaxed cluster. In the case of A523 we considered the biweight position in R.A. and Dec. of the fiducial member galaxies [R.A. $= 04^h59^m08^s.97$, Dec. $= +08°48'06''.3$ (J2000.0)]. The biweight is a robust statistic for determining the central location of a distribution. It was suggested by Tukey (1960) as an improvement for non-Gaussian and contaminated normal distributions and requires an auxiliary scale estimator, the median absolute deviation from the sample median as used in the ROSTAT statistical routines[5] (Beers, Flynn & Gebhardt 1990). We also considered the X-ray centre listed by Böhringer et al. (2000), and the density peak of the *Chandra* X-ray surface brightness as determined in the present study. Independently of the adopted centre, the 'shifting gapper' procedure confirms the 80 fiducial cluster members in the velocity peak. Hereafter we adopt the biweight centre. The projected phase space of member galaxies is shown in Fig. 5 (top panel).

The analysis of the velocity distribution of the 80 cluster members was performed by using the biweight estimators of location and scale as implemented in the ROSTAT statistical routines (Beers et al. 1990). Note that Beers et al. (1990) tested the resistance, robustness, and efficiency of these and other estimators with extensive simulations for a number of common cases realizable in samples of cluster velocities. Following that study and Girardi et al. (1993), we always used the biweight estimator of scale for samples of $n \geq 15$ galaxies and the gapper estimator for samples of $n < 15$ galaxies. In the case of A523, we calculated the mean cluster redshift, $\langle z \rangle = 0.1040 \pm 0.0004$ (i.e. $\langle V \rangle = 31\,165 \pm 107$ km s^{-1}), and the global line-of-sight (LOS) velocity dispersion, $\sigma_V = 949^{+80}_{-60}$ km s^{-1}. The robustness of these estimates with respect to the cluster radius is confirmed by our analysis of the mean velocity and velocity dispersion profiles (see Fig. 5).

3.2 Cluster substructure

We analysed the presence of substructure on the basis of the velocity distribution of galaxies, their projected positions on the sky, and combining these two pieces of information (1D, 2D, and 3D tests). According to the analysis of the velocity distribution, there is no evidence for possible deviations from Gaussianity according to a variety of parameters (kurtosis, skewness, tail index, and asymmetry index; Bird & Beers 1993).

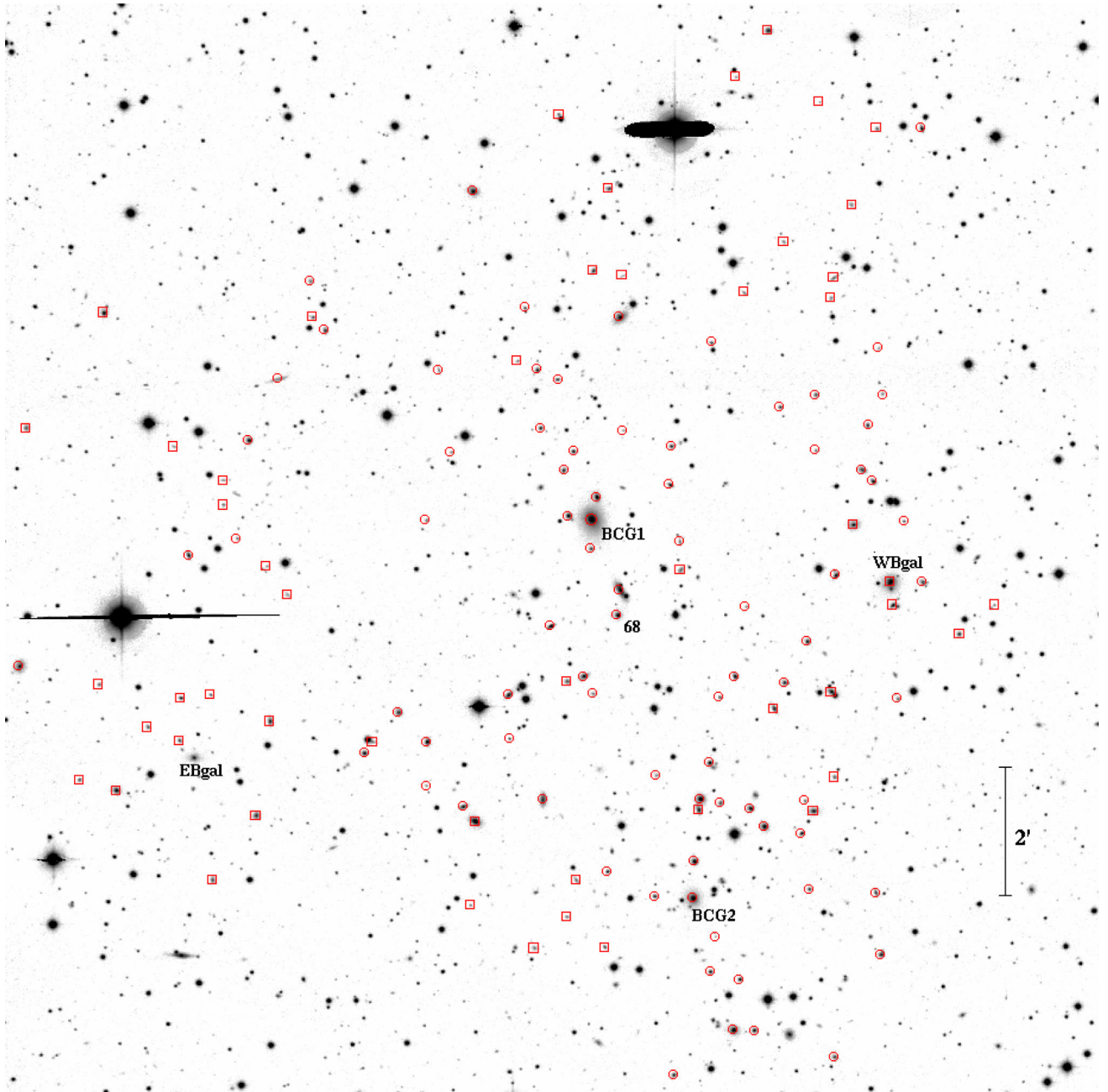[5] http://bima.astro.umd.edu/nemo/man_html/rostat.1.html

Figure 2. INT *r*-band image of Abell 523. Open symbols highlight galaxies of our spectroscopic catalogue. Circles and squares indicate cluster members and non-member galaxies, respectively (see Table 1). Labels refer to specific galaxies discussed in the text. North is up and east is left. The FOV of the image is $2 \times 2 \, h_{70}^{-1}$ Mpc.

We analysed the spatial distribution of the 80 spectroscopic member galaxies by using the 2D adaptive-kernel method of Pisani et al. (1996, hereafter 2D-DEDICA, see also the appendix in Girardi et al. 1996). Our results are presented in Fig. 6 and Table 2 and highlight a SSW-NNE elongated structure with two very significant galaxy peaks. BCG1 and BCG2 are the two dominant galaxies of the northern and southern subclusters, respectively. We also detected a third, low-density peak, at the limit of our detection threshold, in the NW. However, our spectroscopic data do not cover the entire cluster field and are affected by magnitude incompleteness due to unavoidable constraints in the design of the MOS masks. The analysis of the photometric catalogues can offer an unbiased description of the

2D galaxy distribution. On the other hand, in the specific case of A523, the presence of the BACKstruct at $z \sim 0.14$ has to be taken into account (Section 3.3) and the analysis of the INT photometric catalogues is given in Section 3.4.

As for the 3D analysis, we searched for a correlation between velocity and position information checking for a velocity gradient (see e.g. den den Hartog & Katgert 1996; Girardi et al. 1996) and applied the Δ-test by Dressler & Schectman (1988). The Δ-test is a powerful test for 3D substructure (Pinkney et al. 1996). We also used two kinematical estimators alternative to the δ_i parameter of the standard Δ-test (Barrena et al. 2011, see also Girardi et al. 1997). We considered separately the contribution of the devi-
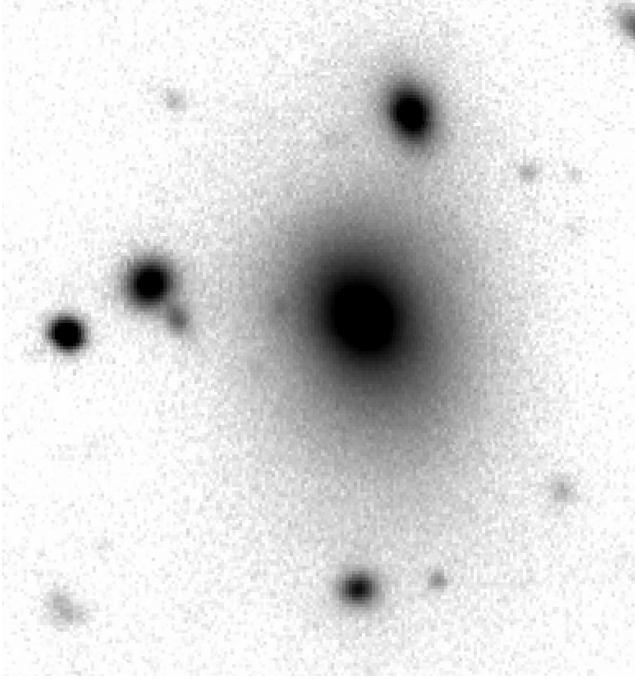
Figure 3. Zoomed-in INT r image to view the details of the halo of BCG1, the brightest cluster galaxy specifically related to the northern subcluster. (The FOV of the image is $\sim 125 \times 130 \, h_{70}^{-1}$ kpc.)
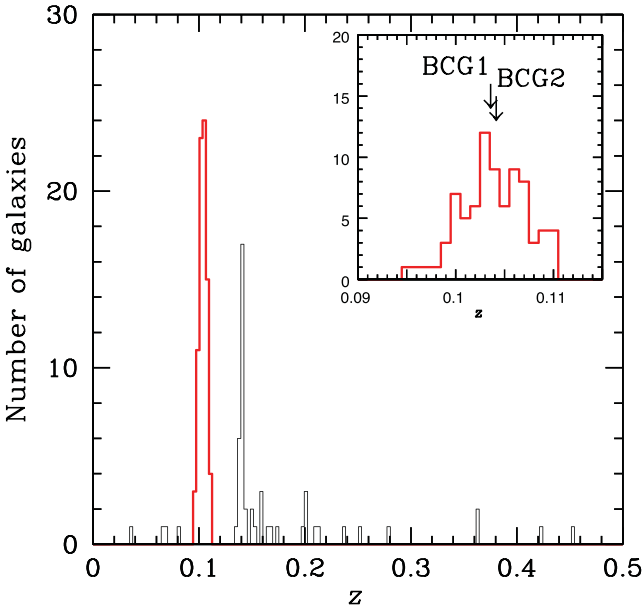
Figure 4. Redshift galaxy distribution. Thick red line histogram refers to the 80 galaxies assigned to A523 according to the 1D-DEDICA reconstruction method. An important background structure at $z \sim 0.14$ (BACKstruct) is also evident in the figure. The inset figure shows the member-galaxy distribution with the indication of the BCG1 and BCG2 velocities.

ation of the local mean velocity from global mean velocity $\delta_{i,\,V} = [(N_{nn} + 1)^{1/2}/\sigma_V](V_{loc} - \langle V \rangle)$ and the contribution of the deviation of the local velocity dispersion from the global velocity dispersion $\delta_{i,\,s} = [(N_{nn} + 1)^{1/2}/\sigma_V](\sigma_{V,\,loc} - \sigma_V)$, where the subscript loc denotes the local quantities computed in the group containing the ith galaxy and its $N_{nn} = 10$ neighbours. In all the above tests, the statistical significance is based on 1000 Monte Carlo simulated clusters
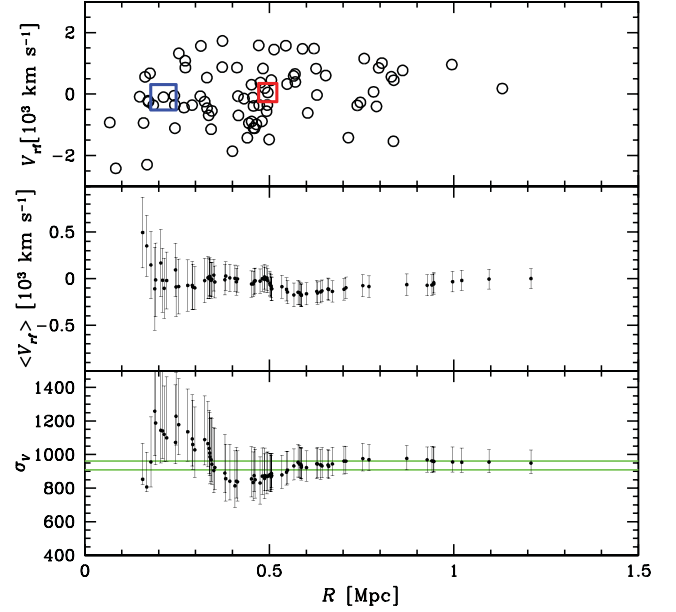
Figure 5. Top panel: rest-frame velocity versus projected clustercentric distance for the 80 member galaxies. The very large blue square indicates BCG1 and the large red square indicates BCG2. Middle and bottom panels: integral profiles of mean rest-frame velocity and LOS velocity dispersion, respectively. The mean (and dispersion) at a given (projected) radius R from the cluster centre is estimated by considering all galaxies within that radius – the first value computed on the five galaxies closest to the centre. The 68 per cent error bands are also shown. Reference values for global mean velocity and velocity dispersion are $\langle V \rangle = 31\,165 \pm 107$ km s^{-1} and $\sigma_V = 949^{+80}_{-60}$ km s^{-1}. In the bottom panel, the horizontal, green line represents the 1sigma error band of the X-ray temperature ($kT_{OUT} = 5.3 \pm 0.3$ keV; see Section 4.3) and converted in σ_V assuming energy density equipartition between ICM and galaxies, i.e. $\beta_{spec} = 1$ (see Section 6).

obtained shuffling galaxies velocities with respect to their positions. In A523 we found no significant evidence for a velocity gradient and substructure. However, in Fig. 7 we show the Dressler & Schectman bubble-plots resulting from the indicator $\delta_{i,\,V}$ for $N_{nn} = 10$ and $N_{nn} = 5$. In fact, these plots are quite suggestive of how BCG1 is surrounded by galaxies having lower velocity than galaxies surrounding BCG2, in agreement with our following analyses.

We performed the 3D-DEDICA analysis detecting two very significant density peaks corresponding to the northern and southern subclusters and having peak velocities of 30 932 and 31 121 km s^{-1}. We also detected two other peaks, still >99 per cent significant, characterized by very high velocities (32 024 and 32 806 km s^{-1}). Due to the problem of combining non-homogeneous quantities like position and velocity, one should be cautious in treating with results coming from methods of 3D reconstruction. However, in the case of A523, both the 3D-DEDICA analysis and the Dressler & Schectman bubble-plot agree in showing a structure more complex than the bimodal one and in finding that the low-velocity galaxy population around BCG1 is surrounded by two populations at high velocity (cf. Fig. 8 and the lower panel in Fig. 7). This complexity is likely the reason why we detected no significant evidence for a velocity gradient and for substructure using classic tests and suggest the need of a larger redshift sample to successfully describe the cluster velocity field.

Although the northern and southern subclusters cannot be separately detected in the velocity distribution, we obtained three alternative estimates of their relative LOS velocity, all indicating that
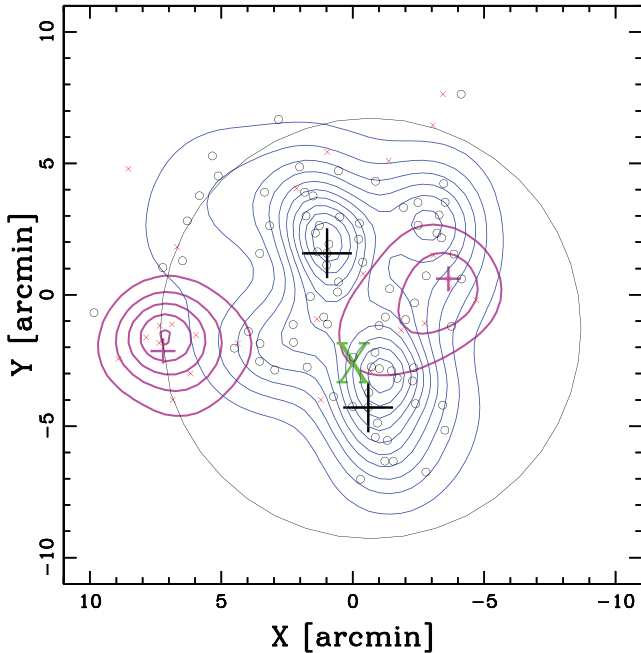
Figure 6. Spatial distribution on the sky of the 80 spectroscopic cluster members and relative isodensity contour map obtained with the 2D-DED-ICA method (small black open circles and thin blue contours). The two huge (black) crosses indicate the position of BCG1 and BCG2 which are close to the NNE and SSW galaxy density peaks, respectively. A third, less dense peak lies in the NW. Thick magenta contours and small red crosses refer to the BACKstruct galaxies and large magenta crosses indicate EB-gal and WBgal, suggested to be two dominant galaxies in the ESE-Bgroup and WNW-Bgroup. The plot is centred on the cluster centre and the circle contains the cluster within a radius equal to 8 arcmin~$0.92\ h_{70}^{-1}$ Mpc ($\sim 0.5 R_{200}$). The large (green) 'X' label indicates the peak of the X-ray surface brightness as determined in this study.

Table 2. Results of the 2D-DEDICA analysis from the spectroscopic sample. For each subsample detected in the z catalogue, the table lists the number of assigned member galaxies N_S, R.A. and Dec. of the density peak, the relative density with respect to the highest peak ρ_S, and χ^2 value of the peak.

Subclump	N_S	α(J2000), δ(J2000) h : m : s, $^\circ$: $'$: $''$	ρ_S	χ_S^2
NNE(z)	40	04 59 12.9+08 50 08	1.00	16
SSW(z)	28	04 59 04.5+08 45 03	0.98	18
NW(z)	12	04 58 57.3+08 50 46	0.58	8

the northern subcluster, related to BCG1, is populated by galaxies having on average a velocity lower than galaxies populating the southern subcluster, related to BCG2. We considered (i) the LOS velocity difference of the BCGs in the cluster rest frame, $\Delta V_{rf} \sim$ 150 km s^{-1}, and (ii) the difference between the two main subsystems detected in the 3D-DEDICA analysis, $\Delta V_{rf} \sim 170$ km s^{-1}. The (iii) estimate is based on the analysis of the mean velocity profiles computed using BCG1 or alternatively BCG2 as centres. Fig. 9 (upper panel) shows that as the galaxy populations surrounding BCG1 and BCG2 within 0.3 h_{70}^{-1} Mpc do differ in their mean velocity, while when considering galaxies at larger radii the mixing of the populations makes the values of the mean velocity to converge to the global value. Considering galaxies at $R \lesssim 0.3\ h_{70}^{-1}$ Mpc,
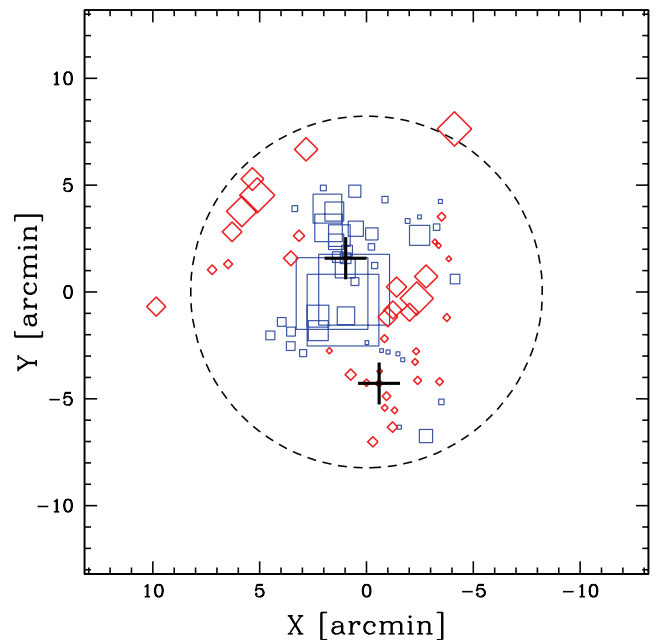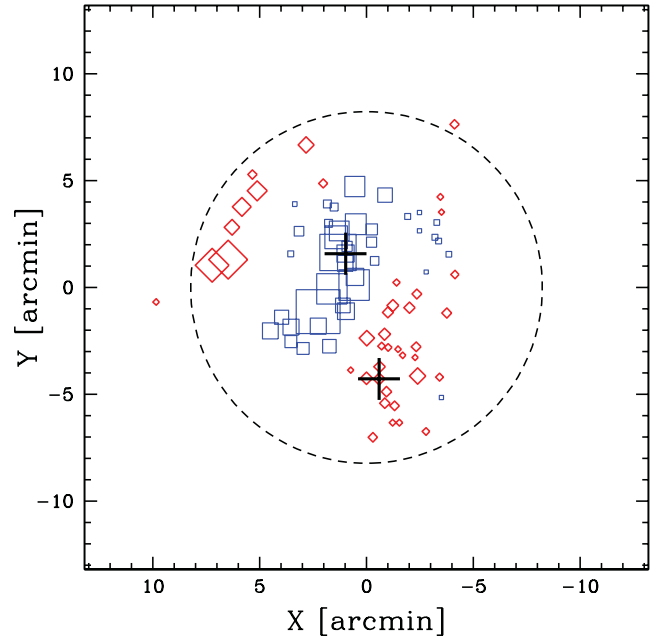

Figure 7. Dressler & Schectman bubble-plot for the Δ-test based on local mean velocities estimated on $N_{nn} + 1$ galaxies. Spatial distribution of the 80 cluster members, each marked by a symbol: the larger the symbol, the larger is the deviation of the local mean velocity from the global mean velocity with scale $\propto \exp(|\delta_{i,\,V}|)$. Thin blue squares and thick red rotated squares show where the local value is smaller or larger than the global value. The plot is centred on the cluster centre and the circle (dashed line) contains the region within a radius equal to 8 arcmin $\sim 0.92\ h_{70}^{-1}$ Mpc. Upper and lower panels refer to the cases $N_{nn} = 10$ and $N_{nn} = 5$, respectively.

we computed $\langle V_N \rangle = 30\,561 \pm 168$ km s^{-1} and $\langle V_S \rangle = 31\,283 \pm$ 137 km s^{-1}, which means a velocity difference significant at the 2.7 sigma c.l. ($\Delta V_{rf} \sim 650$ km s^{-1}).

We also performed the analysis of the velocity dispersion profiles (Fig. 9, lower panel). As for the population around BCG2, galaxies at $R \lesssim 0.3$ are characterized by a low value of velocity dispersion,
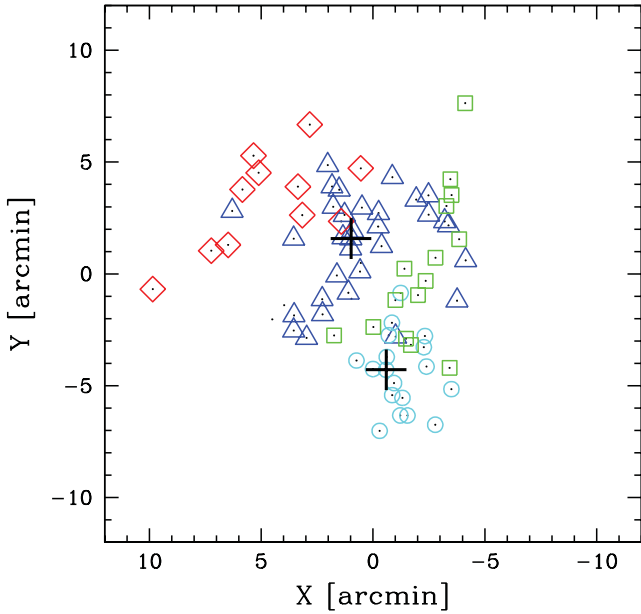
Figure 8. Spatial distribution of the 80 cluster members (small black points) within a region of ∼2.8 × 2.8 h_{70}^{-1} Mpc centred on the cluster centre, where the galaxies of the four subclusters detected in the 3D-DEDICA analysis are indicated by large symbols. Blue triangles, cyan circles, green squares, and red rotated squares indicate galaxies of groups with increasing mean velocities. The group formed of galaxies indicated by cyan circles is the closest one to the mean cluster velocity. The members of the two main subclusters are indicated by blue triangles (the northern one) and cyan circles (the southern one). The northern subcluster stands out for its low velocity being surrounded by two high-velocity groups. The two crosses indicate the two BCGs.
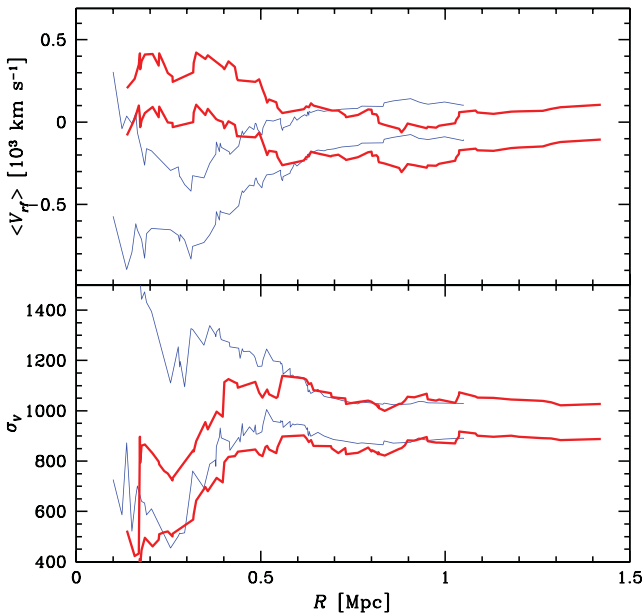
Figure 9. Error bands of mean velocity and velocity dispersion profiles computed as in middle and bottom panels of Fig. 5. Thin blue lines refer to BCG1 as centre and thick red lines refer to BCG2 as centre. The comparison highlights the difference in mean velocity between populations surrounding the two BCGs.

Table 3. The 2D structure of the background structure based on spectroscopic data. For each subsample the table lists the same quantities as in Table 2.

Subclump	N_S	α(J2000), δ(J2000) h : m : s,° : ′ : ″	ρ_S	χ_S^2
ESE-Bgroup	11	04 59 37.9+08 46 30	1.00	6
NWN-Bgroup	10	04 58 55.1+08 48 17	0.58	4

while at larger radii the profile increases likely due to the contamination of the northern subcluster. Thus we can estimate $\sigma_{V, S} \sim$ 650 km s^{-1} for the galaxy population related to BCG2. The population around BCG1 is characterized by a higher nominal value of velocity dispersion, but the huge uncertainty prevents us to give an estimate of $\sigma_{V, N}$.

3.3 The background galaxy structure at $z \sim 0.14$

The BACKstruct is not a dense galaxy system, but rather a quite sparse structure. Applying the 2D-DEDICA analysis to the BACKstruct galaxies we detected two loose overdensities tracing the ESE-WNW direction (ESE-Bgroup and WNW-Bgroup; see Table 3). Fig. 6 shows the relevant contour map (red contours).

The galaxy population of the WNW-Bgroup is dominated by the galaxy ID 8 (WBgal), while the galaxy population of the ESE-Bgroup seems to be related with the bright galaxy located at R.A. = 04^{h}59^{m}38^{s}2, Dec. = +08°45′58″ (J2000.0; EBgal). X-ray emission is associated with both WBgal and EBgal and radio emission with EBgal only (see Fig. 1). As for the WBgal galaxy listed in Table 1, its magnitude refers to a close couple of galaxies/nuclei in the same light halo, and the spectrum refers to the northern galaxy/nucleus. As for the EBgal, this is not listed in our redshift catalogue. However, its colour is typical of that of the background structure and is surrounded by a faint halo and a few small galaxies.

In the effort of understanding the nature of the BACKstruct, we note that A523 is part of the supercluster SCL62 (Einasto et al. 2001) together with Abell 515, 525, 529, 532 in the range of photometric redshifts z_{phot} = 0.04–0.14 (Gal et al. 2000). The BACKstruct might be related to the outskirts, at ∼6 h_{70}^{-1} Mpc, of Abell 525 which is the closest to A523 in the plane of the sky and has $z_{phot} \sim 0.14$.

3.4 2D cluster structure based on the photometric data

Here, we present our results about the cluster structure based on the INT photometric catalogues. We selected photometric members on the basis of both ($r - i$ versus r) and ($g - r$ versus r) colour–magnitude relations (CMRs), which indicate the early-type galaxies locus. The equations of the two CMRs are $r - i$ = 0.904–0.024× r and $g - r$ = 1.613–0.004× r and we selected galaxies within a colour range of 0.1 and 0.15, respectively (see Fig. 10). To determine the CMRs we applied a 2σ-clipping fitting procedure to the spectroscopic members (see Boschin et al. 2012 and references therein). In particular, to reduce the contamination of non-member galaxies, we considered the galaxies with $r \leq 19$, corresponding to ∼2 mag after M^*, for a total of 196 members in the whole photometric catalogue.

The results of the 2D-DEDICA analysis are presented in Fig. 11 and Table 4 and confirm the results obtained in the spectroscopic sample, that is the presence of the northern and southern
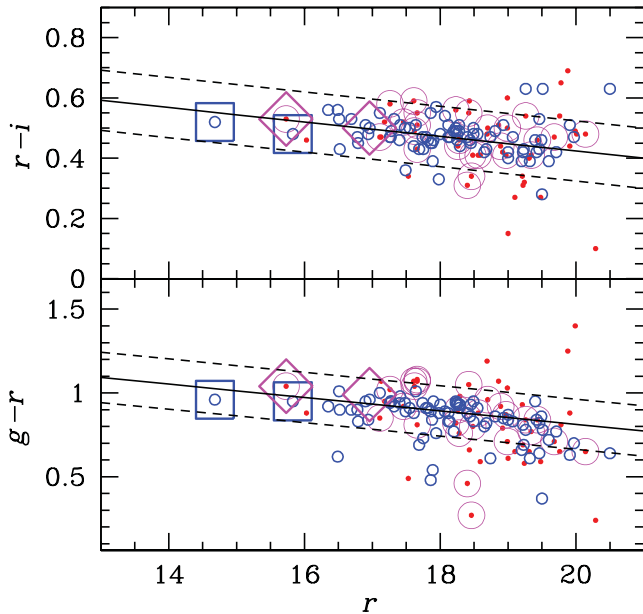
Figure 10. Upper and lower panels: $r - i$ versus r and $g - r$ versus r diagrams, respectively. Galaxies with available spectroscopy are shown by blue open circles (cluster members) and small red dots (field members). Very large, blue open squares indicate BCG1 and BCG2. In both panels the solid line gives the best-fitting CMR as determined on spectroscopic cluster members; the dashed lines define the regions within which photometric cluster members are selected. To stress the problem of contamination in A523 due to the background field, we indicate galaxies belonging to the BACKstruct with large magenta open circles. Very large, magenta open rotated squares indicate WBgal and EBgal, the second one not included in our spectroscopic catalogue.

subclusters, NNE(2D) and SSW(2D) peaks. In addition, we detected S-SSW(2D), a less dense peak in the southern region, poorly sampled by our spectroscopic catalogue, tracing the SSW-NNE direction too. We also detected two minor density peaks, ESE(2D) and WNW(2D), tracing the ESE-WNW direction, but they might be partially or totally spurious, as due to the BACKstruct contamination, as discussed in the following.

Fig. 10 shows that several galaxies of the BACKstruct have colours similar to those of A523 red sequence galaxies thus likely contaminating our catalogue of photometric members. In fact, 21 out of the 26 galaxies of the BACKstruct are (erroneously) classified as photometric members of A523. Therefore, our photometric sample is likely contaminated by the BACKstruct galaxies, in particular in the WNW and ESE regions. The ESE(2D) peak, located in a region where we do not detect any cluster overdensity, might be not related to A523, while the WNW(2D) peak, located in a region where both the WNW-Bgroup of the BACKstruct and the NW(z) of the A523 cluster are projected, might be contaminated (cf. Figs 6 and 11). As for the SSW-NNE region traced by the two main subclusters, we estimated a small ($\lesssim$15 per cent) contamination. This estimate is the ratio of the number of the BACKstruct galaxies classified as A523 photometric members to the number of A523 galaxies (spectroscopic sample) classified as A523 photometric members. Therefore, we expect a small effect in the estimate of the 2D positions of the peaks of the northern and southern subclusters as listed in Table 4 (see also the good agreement with those in Table 2).
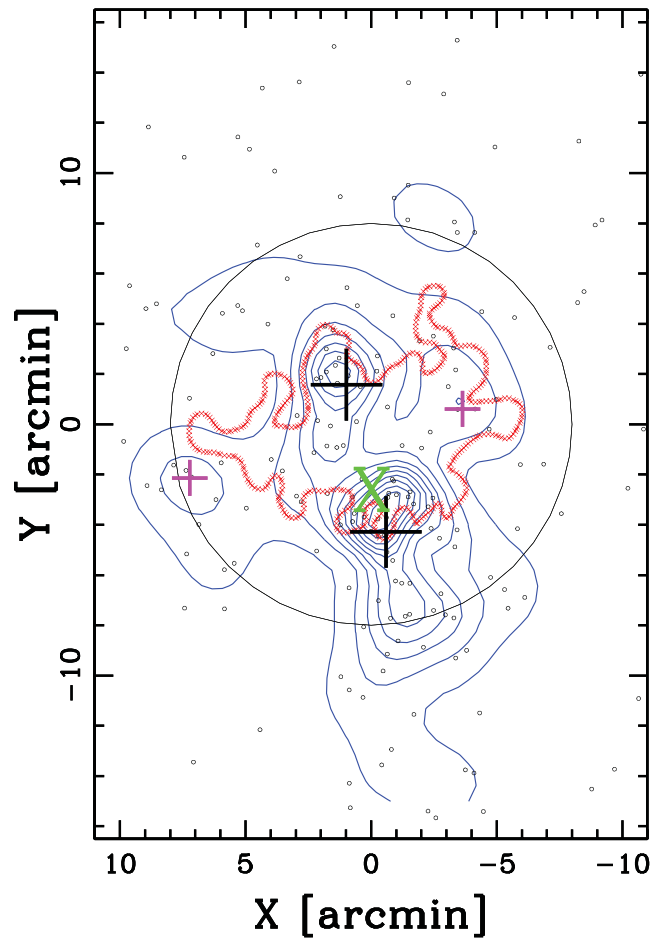

Figure 11. Spatial distribution on the sky of the photometric cluster members with $r \leq 19$ (small black dots). The contour map is obtained with the 2D-DEDICA method (blue contours). The two large black crosses indicate the position of BCG1 and BCG2 and the two magenta crosses indicate EBgal and WBgal, likely the dominant galaxies in the background structure (see Fig. 6 and the text). The radio emission is shown in a schematic way (small red crosses) to give the lowest contour of Fig. 17 (middle panel). The large green 'X' label indicates the peak of the X-ray surface brightness. The plot is centred on the cluster centre and the circle contains the region within a radius equal to 8 arcmin $\sim$0.92 h_{70}^{-1} Mpc.

Table 4. Results of the 2D-DEDICA analysis from the INT photometric sample. For each subsample the table lists the same quantities as in Table 2.

Subclump	N_S	α(J2000), δ(J2000) h : m : s, $^\circ$: $'$: $''$	ρ_S	χ_S^2
SSW(2D)	35	04 59 07.6+08 44 20	1.00	20
NNE(2D)	20	04 59 14.4+08 50 07	0.71	11
S-SSW(2D)	40	04 59 03.4+08 40 58	0.52	12
WNW(2D)	22	04 58 54.3+08 49 00	0.28	7
ESE(2D)	16	04 59 38.3+08 45 49	0.23	7

4 X-RAY MORPHOLOGICAL AND SPECTRAL ANALYSIS

4.1 Observation and data reduction

A523 was observed by *Chandra* with the *ACIS-I* configuration in VFAINT mode on 2013 November 04 (obsID 15321). The data were analysed with *CIAO* 4.6 in conjunction with the *Chandra*

Calibration Database (CALDB) 4.6.1. All data were reprocessed from the level = 1 event files following the standard *Chandra* reduction threads. In particular we ran the task ACIS_PROCESS_EVENTS to flag background events that are most likely associated with cosmic rays and removed them. With this procedure, the ACIS particle background can be significantly reduced compared to the standard grade selection. The data were filtered to include only the standard event grades 0, 2, 3, 4 and 6. From low surface brightness regions of the active chips we extracted light curves which were cleaned from soft proton flares using the *CIAO* task DEFLARE with the CLEAN option. The observation was quiescent resulting in a negligible loss of time and in an effective exposure time of 27 ks. Point source detection was performed using WAVEDETECT on a 0.5–7 keV band image, supplied with a 1.4 keV PSF map to minimize spurious detections at chip boundaries. The detection threshold was set to 10^{-6} and the scales were set to a factor of 2 from 1 to 8. Point sources were removed using appropriate elliptical regions containing 99 per cent of their flux. Spectral extraction was performed with the *CIAO* tool SPECEXTRACT creating the appropriate response files, RMF and ARF, for the selected spatial region. Spectral fitting was performed with XSPEC 12.8.2 using the C-statistic. We rebinned the spectra to ensure at least 20 photons per bin to aid in model selection and computational speed. The energy range was restricted to 0.5–7.0 keV and all spectra were fitted including components for the cluster emission and background. We used a single thermal APEC component to model the ICM emission modified by Galactic absorption fixed at 1.2×10^{21} cm^{-2} (Dickey & Lockman 1990; a similar value 1.05×10^{21} cm^{-2} is reported by Kalberla et al. 2005). To account for the background we included additional spectral components in the fits: we included two APEC components ($kT = 0.07$ keV and 0.2 keV, the former un-absorbed) to account for the Galactic foreground and a power-law component ($\Gamma = 1.41$) for the Cosmic X-ray Background due to unresolved AGNs. To account for the instrumental background, we followed the analytical model of Bartalucci et al. (2014) which was not folded through the ARF. The background parameters were constrained by fitting spectra extracted from regions free of cluster emission at the edges of the FOW, and then the fitted normalizations were rescaled accordingly to the source extraction area.

4.2 X-ray image and surface brightness analysis

We created an image in the 0.5–7 keV band and a corresponding exposure map at 1.4 keV, to make an exposure-corrected image, smoothed on a scale of 10 arcsec, as shown in Fig. 12. We processed the image to remove the point sources using the CIAO tool DMFILTH, which replaces photons in the vicinity of each point source with a locally estimated background. We performed a morphological analysis adopting quantitative measures by applying the power ratios technique (Buote & Tsai 1996), the centroid shifts (Mohr, Fabricant & Geller 1993) and the concentration parameter (Santos et al. 2008). The power ratio method exploits the idea that the X-ray surface brightness represents the projected mass distribution of the cluster. The power ratio is a multipole decomposition of the two-dimensional surface brightness inside a given aperture. We calculated the power ratios within an aperture of $500\,h_{70}^{-1}$ kpc for comparison with previous work. In particular, we used the P_3/P_0 ratio which provides a clear substructure measure following Cassano et al. (2010). Centroid shifts indicate that the centre of mass of the X-ray emitting gas varies with radius. Centroid shifts and power ratios are both capable of identifying highly disturbed systems or systems with significant, well-defined substructures (Poole et al.
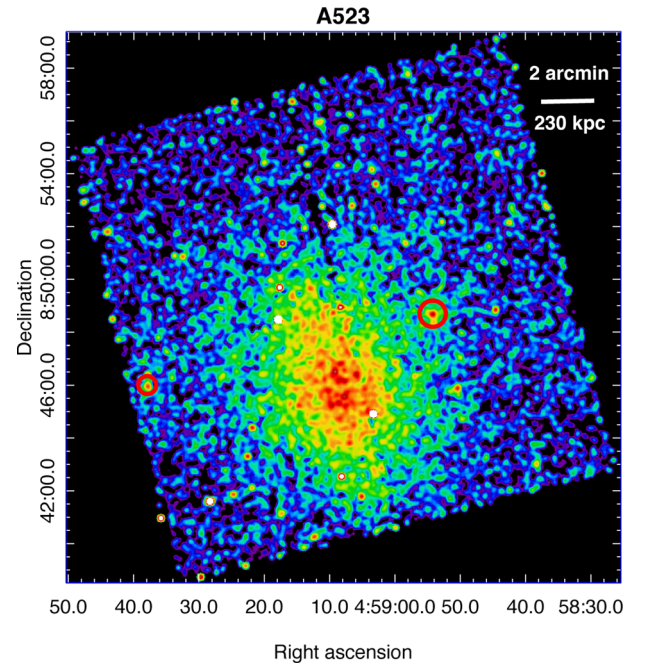

Figure 12. *Chandra* image in the 0.5–7 keV energy band smoothed on a 10 arcsec scale. The image was divided by the exposure map at 1.4 keV to correct for exposure variations. The detected point sources connected with galaxies belonging to the background groups are highlighted by two red open circles.

Table 5. Results of the morphological analysis of the X-ray image of A523. The table lists the power ratio P_3/P_0; the centroid shift w as computed within a radius of ($500\,h_{70}^{-1}$ kpc); the concentration parameter c. All the three indicators indicate that A523 is a disturbed cluster.

P_3/P_0 ($\times 10^{-7}$)	w ($500\,h_{70}^{-1}$ kpc)	c
$1.8^{+2.3}_{-1.6}$	0.025 ± 0.002	0.095 ± 0.003

2006). Following the method of Poole et al. (2006), the centroid shift was computed in a series of circular apertures centred on the cluster X-ray peak. The radius of the apertures was decreased in steps of 5 per cent from $500\,h_{70}^{-1}$ kpc to $25\,h_{70}^{-1}$ kpc. The concentration parameter, c, is defined as the ratio of the peak (calculated within $100\,h_{70}^{-1}$ kpc) over the ambient surface brightness (calculated within $500\,h_{70}^{-1}$ kpc). The concentration parameter differentiates clusters with a compact core (core not disrupted by a recent merger event) from clusters with a spread distribution of gas in the core (core disrupted by a recent merger episode).

We applied these techniques and the results are reported in Table 5. All the morphological indicators confirm quantitatively the simple visual indication of a disturbed cluster affected by a merger.

We extracted the surface brightness profile from the exposure-corrected image in the 0.5–7 keV band and accounted for the X-ray background by including a constant background component. The data were grouped to have 200 counts per bin and the χ^2 statistics was applied. The best-fitting β-model has a core radius of $r_c = (181 \pm 17)\,h_{70}^{-1}$ kpc (i.e. 98 $\pm$10 arcsec) and $\beta = 0.42 \pm 0.02$ for a χ^2/d.o.f. = 116/115 (see Fig. 13). The peak of the surface brightness lies at R.A. = $04^h59^m08\overset{s}{.}9$, Dec. = $+08°45'31''$ (J2000.0) and the
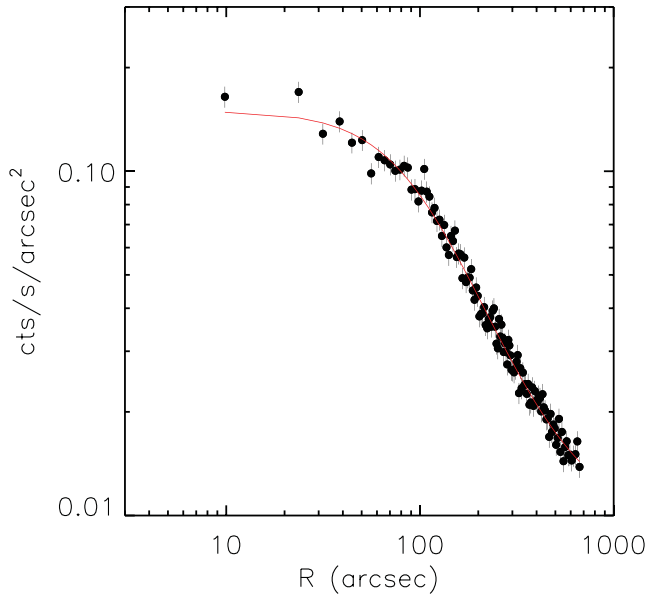
Figure 13. Surface brightness profile of the X-ray emission of A523. The best-fitting β-model is also shown in red.

central gas density, as obtained in a region of 165 h_{70}^{-1} kpc, is 1.1×10^{-3} cm^{-3} with an uncertainty of 4 per cent.

4.3 Spectral analysis

We calculated the mean temperature of the cluster as the temperature obtained with a spectral fit in the region $0.05R_{180} < r < 0.2R_{180}$, where $R_{180} = 1780(kT/5\,\text{keV})^{1/2}h(z)^{-1}$ kpc with $h(z) = (\Omega_M(1 + z)^3 + \Omega_\Lambda)^{1/2}$ using an iterative procedure to calculate kT and R_{180} (Rossetti & Molendi 2010). We found $kT = 5.3 \pm 0.3$ keV. The value of kT thus estimated within the $0.05R_{180} < r < 0.2R_{180}$ region, hereafter kT_{OUT}, is a good proxy for the global temperature (see fig. 4 of Leccardi & Molendi 2008 where kT_M is the global temperature).

We also prepared a coarse two-dimensional map of X-ray temperature, using the contour binning technique of Sanders (2006) with a signal-to-noise ratio of 50, which resulted in three interesting regions shown in Fig. 14. The values for the temperatures are $kT_{\text{Reg2}} = 4.7 \pm 0.4$ keV in the central region, $kT_{\text{Reg1}} = 6.6 \pm 0.9$ keV in the northern region, and $kT_{\text{Reg3}} = 4.7 \pm 0.5$ keV in the southern region.

4.4 X-ray luminosity estimate and the L_X–T relation

The previously available X-ray information for this cluster is limited to a *ROSAT* All Sky Survey observation which detected the cluster at a flux of $F_X = 4.5 \times 10^{-12}$ erg cm^{-2} s^{-1} in the 0.1–2.4 keV band, bright enough to be included in the *ROSAT* BCS (Ebeling et al. 1998), with a predicted temperature of 4.3 keV (see their table 3). Based on the *ROSAT* data Böhringer et al. (2000, NORAS Survey) list a luminosity $L_X(< R_{ap} = 0.92\ h_{70}^{-1}\ \text{Mpc}) = 0.88 \times 10^{44}$ h_{70}^{-2} erg s^{-1} in the 0.1–2.4 keV band which, as standardized in the MCXC catalogue (Piffaretti et al. 2011), gives a luminosity of $L_{X, 500} = 0.91 \times 10^{44}$ h_{70}^{-2} erg s^{-1} in the 0.1–2.4 keV band, within the radius[6] $R_{500} = 0.83\ h_{70}^{-1}$ Mpc.

---

[6] The radius R_δ is the radius of a sphere with mass overdensity δ times the critical density at the redshift of the galaxy system.
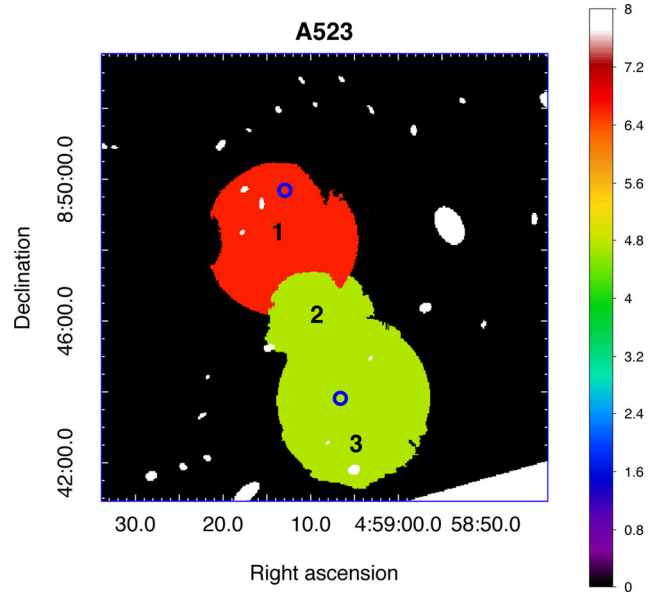
Figure 14. Temperature map (keV) showing that the northern cluster region is characterized by a higher temperature than the central and southern regions. The central 1.5 arcmin radius region, indicated by the label '2', is centred close to the X-ray peak, precisely at R.A. = $04^h59^m09\overset{s}{.}0$, Dec. = $+08°45'55''$ (J2000.0). The FOV of the image is ~1.5 × 1.5 h_{70}^{-1} Mpc. The two small blue circles indicate BCG1 and BCG2 in the northern and southern regions (regions 1 and 3, respectively).

This value corresponds to a predicted temperature of 2.9 keV using the best-fitting L_X–T relation found in REXCESS (appendix B of Pratt et al. 2009). These predicted temperature estimates are significantly lower than our measure of the X-ray temperature based on *Chandra* data suggesting that A523 may be a significant outlier in the L_X–T relation (see Fig. 16). To investigate this point we made our own estimate of the A523 X-ray luminosity based on *Chandra* data.

For the luminosity calculation we extracted a spectrum from the entire aperture of radius $0.2R_{180}$ corresponding to 337 h_{70}^{-1} kpc. From the best-fitting model (cstat/d.o.f. = 284/262; see Fig. 15) the unabsorbed flux in the 0.1–2.4 keV band is $2.01 \pm 0.04 \times 10^{-12}$ erg cm^{-2} s^{-1}, which corresponds to an unabsorbed luminosity of $4.84 \pm 0.09 \times 10^{43}$ h_{70}^{-2} erg s^{-1} in the rest-frame band 0.1–2.4 keV. The quoted errors on flux and luminosity were obtained with XSPEC using a Monte Carlo procedure. Assuming that the cluster emission profile follows the best-fitting β-model derived above, the luminosity within $R_{500} = 1100\ h_{70}^{-1}$ kpc, as estimated from the Arnaud, Pointecouteau & Pratt (2005) scaling relation, is $L_{X, 500} = 1.57 \pm 0.14 \times 10^{44}$ h_{70}^{-2} erg s^{-1} in the 0.1–2.4 keV rest-frame band. Errors in the luminosity were determined including both the spectral errors and the uncertainties in the β-model parameters. The aperture of 337 h_{70}^{-1} kpc used as reference contains 31 per cent of the total luminosity estimated within R_{500}. The revised upward *Chandra* luminosity makes A523 more consistent with the envelope of the non-cool-core clusters in the L_X–T relation as shown in Fig. 16.

5 ANALYSIS OF RADIO DATA

5.1 Radio images

We re-analysed archival VLA data at 1.4 GHz in C-array and D-array configuration (AB1180 and AR690 projects). These data had
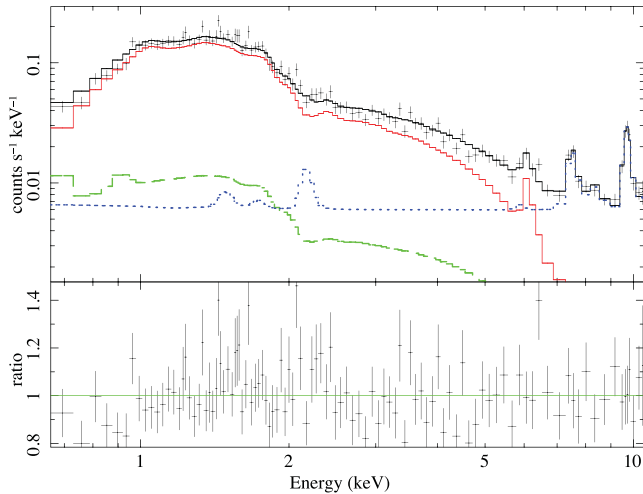
Figure 15. Upper panel: X-ray spectrum of the source taken from a 337 h_{70}^{-1} kpc aperture. The ACIS-I data are shown in black together with the best-fitting model with the cluster component in red (solid line), the particle background in blue (dotted line) and the sky background in green (dashed line). Lower panel: the ratio of the data over the model is also shown.
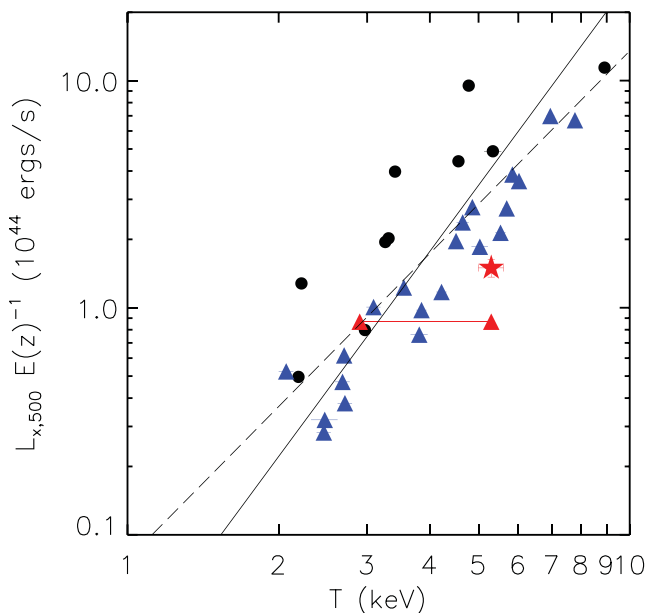
Figure 16. L_X–T relation for the REXCESS sample with quantities derived from all the emission interior to R_{500} in the 0.1–2.4 keV band. Black points represent cool-core systems whereas blue triangles represent non-cool-core systems according to the classification of Pratt et al. (2009). The best-fitting power-law relation derived from BCES (Y|X) (dashed line) and BCES orthogonal (solid line) is overplotted. The two connected (red) triangles represent the position of A523 based on the *ROSAT* luminosity estimate and the predicted value of $T = 2.9$ keV (triangle on the left) and the *Chandra* temperature estimate (triangle on the right). The red star represents the position of A523 based on the *Chandra* temperature and luminosity estimates.

been published in G11 and van Weeren et al. (2011b). For this study, we also considered the polarization information available from the AR690 project. The data were reduced following standard procedures using the NRAO's Astronomical Image Processing System (AIPS) package.

In Fig. 17 (top panel) we present an image at a relatively high resolution (24.4 × 23.2 arcsec², PA = −42°), where the central
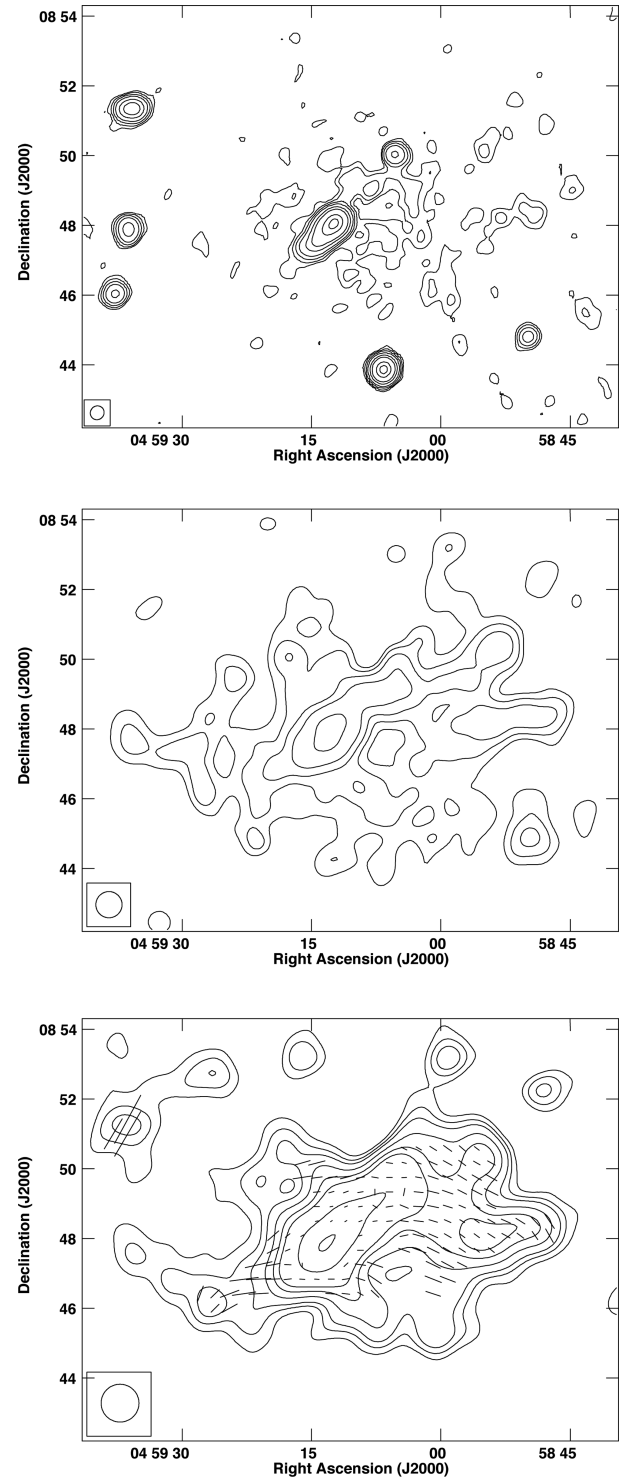
Figure 17. Top panel: total intensity contours at 1.4 GHz with a FWHM of 24.4 × 23.2 arcsec² (PA = −42°). The contour levels are drawn at: 0.025, 0.05, 0.1, 0.2, 0.5, 1, 3, 5 mJy beam⁻¹. The sensitivity (1σ) is 0.012 mJy beam⁻¹. Middle panel: total intensity contours at 1.4 GHz with a FWHM of 45 × 45 arcsec². The contour levels are drawn at: 0.2, 0.5, 1, 2, 5, 10 mJy beam⁻¹. The sensitivity (1σ) is 0.07 mJy beam⁻¹. Bottom panel: total intensity contours and polarization vectors at 1.4 GHz with a FWHM of 65 × 65 arcsec². The contour levels are drawn at: 0.2, 0.4, 0.6, 1, 1.5, 2, 4, 6 mJy beam⁻¹. The sensitivity (1σ) is 0.1 mJy beam⁻¹. The lines give the orientation of the electric vector position angle (E-field) and are proportional in length to the FPOL (1 arcsec ≃ 1.25 per cent). In all the panels, the FOV of the image is ∼1.8 × 1.4 h_{70}^{-1} Mpc.

head–tail radio galaxy is clearly visible as well as the central region of the diffuse emission. Other point-like sources are present. The image noise level is 0.012 mJy beam^{-1}. From this image it is clear that no connection is present between the radio tail and the diffuse emission (cf. with Fig. 17, middle panel).

In Fig. 17 (middle panel) we present an image at a resolution of 45 ×45 arcsec^2 with the discrete sources subtracted. The image noise level is 0.07 mJy beam^{-1}. The discrete sources were subtracted in the (u, v) plane by using the AIPS task UVSUB. This image confirms the presence of a diffuse low-surface brightness radio emission at the cluster centre. The total flux density at 1.4 GHz is 72±3 mJy. This flux density value corresponds to a radio power of $P_{1.4\,GHz}$ = 1.98×10^{24} W Hz^{-1}. The quoted error on the flux density not only is due to the noise but also includes uncertainties in the source subtraction and in the source size. The source angular size is $\simeq 11 \times 8$ arcmin^2.

In Fig. 17 (bottom panel), we present a total intensity image and polarization vectors at a resolution of 65×65 arcsec^2 with the discrete sources subtracted. The image noise level is 0.1 mJy beam^{-1}. The vectors give the orientation of the electric vector position angle (E-field) and are proportional in length to the fractional polarization (FPOL). In the FPOL image we considered as valid those pixels where the FPOL was above $3\sigma_{FPOL}$.

From a detailed analysis of the radio morphology of the diffuse emission, we can derive the following conclusions. (i) There is no connection among discrete sources and the diffuse source. In particular, the head–tail galaxy located close to the centre of the extended source is elongated on the opposite side with respect to the brightest region of the diffuse source (see Fig. 17, top panel). (ii) The residuals from the subtraction of discrete sources are at a very low level and do not affect the diffuse source properties (compare Fig. 17, top and middle panels). (iii) The diffuse source is generally elongated along the ESE-WNW direction. In addition, a

SSW-NNE elongation is present. The radio emission shows an irregular shape, with a filamentary structure characterized by a bright ridge close to the centre. However, there is no evidence of a transverse flux asymmetry as usually found in relic sources due to the propagation of a shock wave (see Feretti et al. 2012). Moreover, as clearly seen in Fig. 17 (top panel), this bright ridge is completely resolved increasing the angular resolution and no compact feature is present, contrary to most of the classic relics found so far (see Feretti et al. 2012 and references therein).

Therefore, in the following section we assume that the diffuse radio source in A523 is a radio halo. More specifically, we suppose that the synchrotron plasma permeates the entire cluster volume rather than being confined to a thin-layer in the peripheral region as in the case of a radio relic. Under this assumption and considering the polarization associated with the radio halo, we analysed the properties of the total intensity and polarized emission with the help of numerical simulations performed with the software FARADAY (Murgia et al. 2004), and we compared the results with the properties of the other radio haloes known in the literature.

5.2 Radio brightness profile

In the left panel of Fig. 18 we show the azimuthally averaged radio halo brightness profile of A523 obtained from the lower resolution (FWHM = 65×65 arcsec^2) image with the discrete sources subtracted. Each data point represents the average brightness in concentric annuli of 30 arcsec (about half beam width), centred on the radio centroid.

We modelled the radio brightness profile, $I(r)$, with an exponential of the form $I(r) = I_0 e^{-r/r_e}$, whose best fit is shown in the left panel of Fig. 18. The proposed method for deriving the radio brightness and the length scale of diffuse emission (Murgia et al. 2009) is relatively independent of the sensitivity of the radio observation.
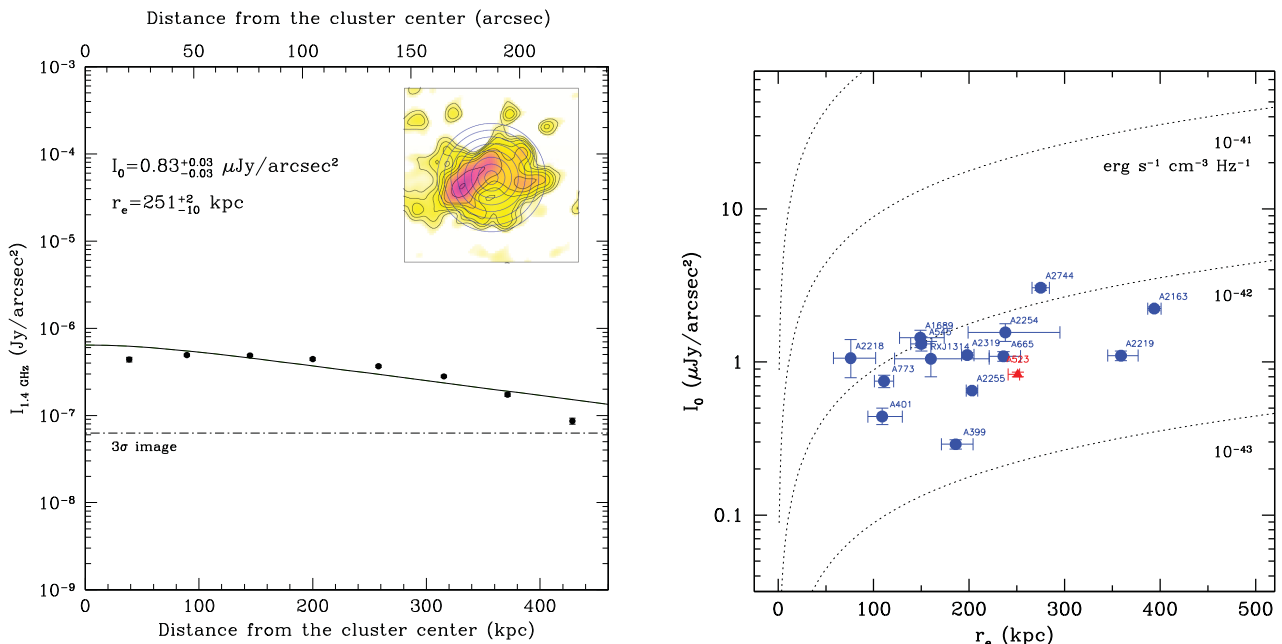

Figure 18. Left panel: the azimuthally averaged brightness profile of the radio halo emission in A523. The profile has been calculated in concentric annuli centred on the radio centroid, as shown in the inset panel. The horizontal dashed-dotted line indicates the 3σ noise level of the radio image, while the continuous line indicates the best-fitting profile described by an exponential law. Right panel: best-fitting central brightness I_0 at 1.4 GHz versus the length scale r_e of A523 in comparison with azimuthally averaged brightness profiles of radio haloes taken from the literature (Murgia et al. 2009, 2010; Vacca et al. 2011, and references therein). The dotted lines indicate regions of constant synchrotron emissivity.

The exponential model is attractive in its simplicity and involves a minimal set of free parameters but, obviously, it cannot account for the local deviations from the circular symmetry of the diffuse emission. The best fit of the exponential model yields a central brightness of $I_0 = 0.83$ μJy arcsec^2 and a length scale $r_e = 251 \pm 10\ h_{70}^{-1}$ kpc.

In the right panel of Fig. 18, we show I_0 versus r_e of A523 in comparison with a set of radio haloes analysed in the literature (Murgia et al. 2009, 2010; Vacca et al. 2011). As previously pointed out, radio haloes can have quite different length scales, but their emissivity is remarkably similar from one halo to another. A523 populates the same region of the I_0–r_e plane as the other radio haloes. Therefore, the diffuse total intensity emission of A523 seems in good agreement with the extrapolation of the properties of the other radio haloes known in the literature.

Morphological similarities between radio and X-ray images have been found in a number of clusters hosting a radio halo (Govoni et al. 2001a) and one feature of A523 is that the point-to-point radio and X-ray emission appears quite different (see also Section 1 and references therein). However, other irregular and asymmetric haloes have been found in the literature (Govoni et al. 2012). Feretti et al. (2012) investigated the statistics of the offset between the peak of the radio halo and of the X-ray emission of the cluster. They have found that the offsets can reach several kpc and they become more relevant for haloes of smaller size. A possible explanation for this behaviour can be attributed to the cluster magnetic field power spectrum. Indeed, magnetic field simulations (Murgia et al. 2004; Govoni et al. 2006; Vacca et al. 2010) show that clusters having most of the magnetic field energy on large spatial scales may produce radio haloes characterized by comparatively high polarization emission with a filamentary structure. Instead, unpolarized radio haloes with a regular morphology are expected in clusters in which most of the magnetic field energy is on small spatial scales. In agreement with the simulation expectations, filaments of polarized emission associated with a radio halo have been detected in A2255 (Govoni et al. 2005) and MACS J0717.5+3745 (Bonafede et al. 2009).

In addition to the radio brightness profile of the total intensity, in Fig. 19 we show the observed brightness profiles of the polarized intensity and FPOL calculated in concentric annuli, as shown in Fig. 18. The observed profiles are traced up to a projected distance from the cluster centre of $\simeq 450\ h_{70}^{-1}$ kpc. The FPOL profile is rather constant at $\simeq$15–20 per cent.

To investigate if the observed FPOL levels and the distorted structure of A523 can be observed in a radio halo, we simulated 3D magnetic fields with a single power-law power spectrum of the magnetic field fluctuations $|B_k|^2 \propto k^{-n}$ with a Kolmogorov spectral index $n = 11/3$. We generated synthetic radio halo images by illuminating 3D magnetic field models with a population of relativistic electrons. At each point, on the computational grid, we calculated the total intensity and the intrinsic linear polarization emissivity at 1.4 GHz, by convolving the emission spectrum of a single relativistic electron with the particle energy distribution of an isotropic population of relativistic electrons. The polarization images were obtained by taking into account that the polarization plane of the radio signal is subject to the Faraday rotation as it traverses the magnetized ICM. We modelled the gas density of A523 with the β-model parameters $r_c = 181\ h_{70}^{-1}$ kpc, $\beta = 0.42$, and a central gas density of $n_0 = 1.1 \times 10^{-3}$ cm^{-3} (see Section 4.2).

The results of the simulations are presented in Fig. 19. By adopting a Kolmogorov spectral index for the magnetic field fluctuations and by considering a magnetic field which decreases with the gas density as $B(r) \propto n_e(r)^{0.5}$, the FPOL levels can be well reproduced by a magnetic field with a central strength $B_0 \simeq 0.5$ μG which fluctuates in a range of scales from a few h_{70}^{-1} kpc up to $\sim 1\ h_{70}^{-1}$ Mpc. The continuum line and the shade region describe the mean and the sigma of a set of simulations (with different random seeds) performed with the magnetic field model described above. The total intensity depends on both the magnetic field and the population of relativistic electrons, while the FPOL mostly depends on the cluster magnetic field correlation-length and strength. Once constrained the magnetic field on the basis of the FPOL profile, it is possible to investigate the population of relativistic electrons. By assuming the equipartition between magnetic field and relativistic electrons, the profiles can be well described by assuming a population of relativistic electrons with an electron energy spectral index $\delta = 3$, and a low- and high-energy cut-offs of the energy spectrum of $\gamma_{\min} = 3500$ and $\gamma_{\max} = 1.5 \times 10^4$, respectively.

In the middle panels of Fig. 19 we show an example of a full resolution total intensity (left) and polarized intensity (right) image obtained with the above magnetic field model. In the bottom panels of Fig. 19 we show as the simulated radio halo would appear when observed at the same resolution 65 arcsec and sensitivity (0.1 mJy beam^{-1}) of A523.

Therefore, we can conclude that a magnetic field model with a central strength $B_0 \simeq 0.5$ μG which fluctuates over a large spatial scale is able to explain the presence of a polarized radio halo at a level of 15–20 per cent characterized by a distorted radio morphology with a significant displacement from the X-ray gas distribution. In the simulation shown in Fig. 19 the radio/X-ray displacement is $\simeq 80\ h_{70}^{-1}$ kpc.

6 SUMMARY OF RESULTS AND DISCUSSION

We present new insights into the structure of the A523 galaxy cluster from our multiwavelength analysis. The main results obtained from optical, X-ray, and radio data are summarized in the following and then discussed to derive a scenario consistent with the available observational picture.

6.1 Results from our multiwavelength analysis

On the basis of 80 member galaxies, we present the first measure of the mean cluster redshift $\langle z \rangle = 0.1040 \pm 0.0004$ – previously only z_{BCG1} was available – and of the LOS velocity dispersion of the galaxy population $\sigma_V = 949^{+80}_{-60}$ km s^{-1}. Our analysis of both spectroscopic and photometric optical data confirms the bimodal structure of the cluster elongated in the SSW-NNE direction, as already suggested by the analysis of old plate images (G11), with the two subclusters $\sim 0.75\ h_{70}^{-1}$ Mpc apart in the plane of sky. We confirm that the northern subcluster is dominated by BCG1, the brightest cluster galaxy, and identify BCG2 as the dominant galaxy that lies in the southern cluster. The redshift data allow us to detect that the two subclusters are (little) separated in the velocity space and we estimate the relative LOS velocity $\Delta_{V,\mathrm{rf}} = 100$–650 km s^{-1} in the cluster rest frame. Suggestions for a more complex structure come from the analysis of the spectroscopic and photometric samples, in particular for one or two clumps tracing the NW-SE (or NWN-ESE) direction (see Figs 6, 8 and 11).

The analysis of *Chandra* data allows us to support with quantitative measures the visual indication of a disturbed cluster already reported by G11 on the basis of *ROSAT* data. The hot ICM structure is now much better defined. The X-ray surface brightness is quite elongated towards NNE, but there is no longer evidence of bimodality (cf. our Fig. 12 and fig. 1 of G11). The peak of the surface
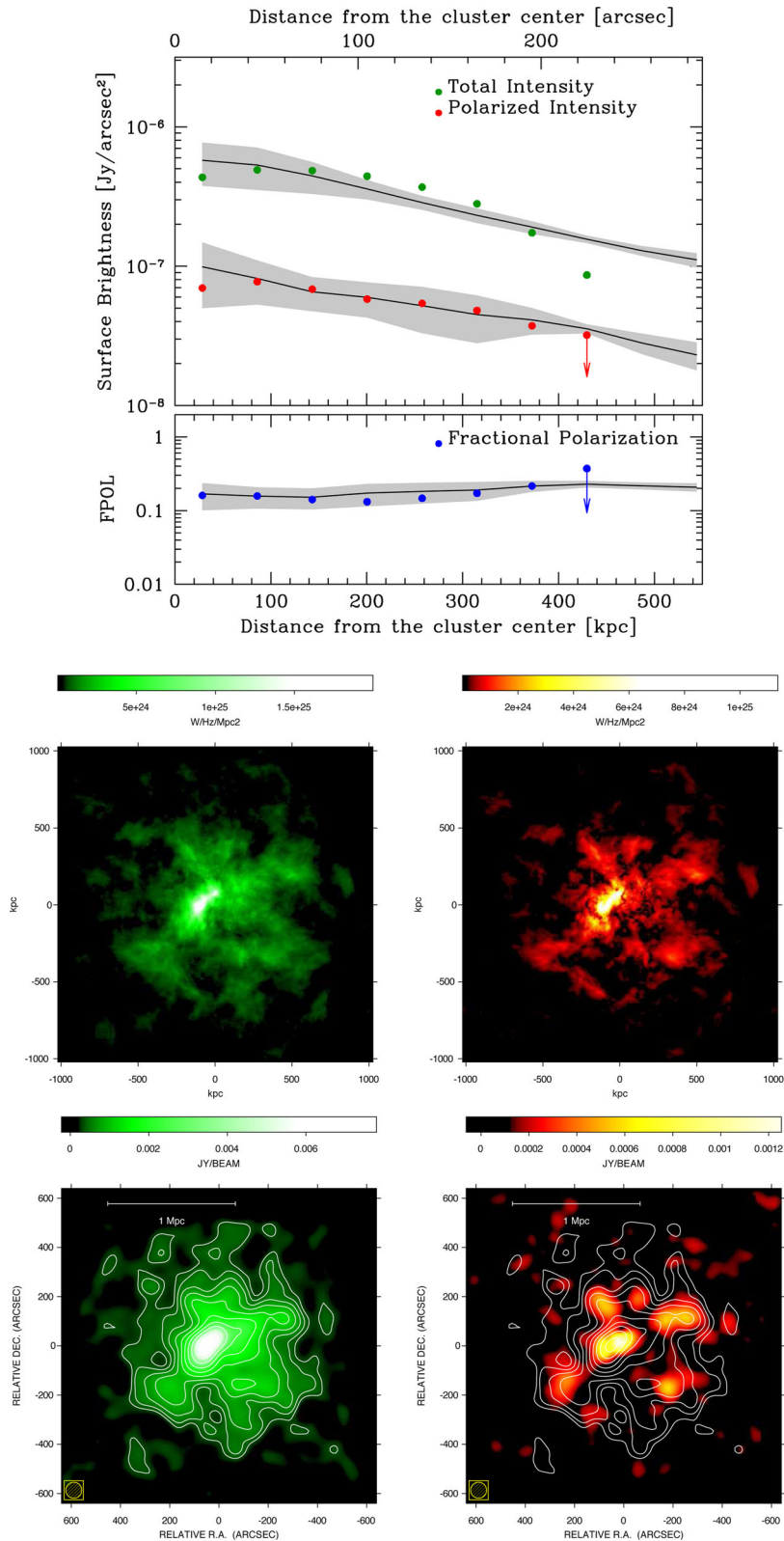
Figure 19. Top panels: azimuthally averaged radio-halo brightness profiles of the total intensity *I* (green dots), polarized intensity *P* (red dots), and FPOL (blue dots). The profiles have been calculated in concentric annuli, as shown in Fig. 18. The continuum line and the shade region in the top panels describe the mean and the sigma of a set of simulations with different random seeds performed with a magnetic field model which is able to describe the data quite well. This model is a Kolmogorov magnetic field power spectrum with a central magnetic field strength of 0.5 μG which fluctuates in a range of scales from a few h_{70}^{-1} kpc up to ∼1 h_{70}^{-1} Mpc and decreases with the gas density as $B(r) \propto n_e(r)^{0.5}$. Middle panels: example of a simulated radio halo at full resolution obtained with the above magnetic field model. Left and right panels refer to the total intensity and polarized surface brightness images, respectively. Bottom panels: the images show as the simulated radio halo would appear when observed at the same resolution and sensitivity of A523. The white contour levels refer to the total intensity image at 65 arcsec resolution. Contour levels start at 0.3 mJy beam^{-1} and increase by a factor of $\sqrt{2}$.

brightness is clearly offset with respect to both the two BCGs, $\lesssim 0.5$ and $\lesssim 0.2\ h_{70}^{-1}$ Mpc from BCG1 and BCG2, respectively. We present the first measure of the global X-ray temperature, $kT_{OUT} = 5.3 \pm 0.3$ keV, and find no evidence for a cool core. Very interestingly, the kT map shows evidence for a higher temperature in the northern region. Our new measure of the X-ray luminosity, $L_{X, 500} = 1.6 \times 10^{44}\ h_{70}^{-2}$ erg s^{-1} in the 0.1–2.4 keV rest-frame band, makes A523 more consistent with the observed L_X–T relation with respect to the previous *ROSAT* estimate, although still lying in the low-luminosity regions of the envelope (see Fig. 16).

Our analysis of VLA data confirms the presence of an extended, diffuse radio source having a maximum projected size of LLS $\sim 1.3\ h_{70}^{-1}$ Mpc. The revised estimate of the radio power, $P_{1.4\,GHz} = 2.0 \pm 0.1 \times 10^{24}$ W Hz^{-1}, is slightly higher than the G11 estimate. Very interestingly, in addition to the main ESE-WNW elongation, our new analysis shows that the radio source has a minor SSW-NNE elongation almost aligned with the main optical/X-ray cluster elongation (see Fig. 17, middle panel, and Fig. 1). The radio source permeates the region between the two subclusters and is classified as a radio halo. In comparison to other clusters hosting radio haloes, A523 is highly peculiar in the $P_{1.4\,GHz}$–L_X plane having a higher radio power (or lower X-ray luminosity) than expected (see also Section 6.4). Despite this, A523 is typical among clusters hosting radio haloes since it populates the same region of the I_0–r_e plane (see Fig. 18, right panel) and the $P_{1.4\,GHz}$–LLS plane (see e.g. fig. 7 of Feretti et al. 2012). The radio emission is clearly offset from the X-ray emission and the radio/X-ray peaks offset is $\sim 0.3\ h_{70}^{-1}$ Mpc. We also detect a modest polarization (FPOL ~ 15–20 per cent), unusual in radio haloes since, so far, a polarized signal has been detected only in a couple of other radio haloes. Both the observed radio/X-ray offset and polarization might be the result of having most magnetic field energy on large spatial scales as we show using an ad hoc set of simulations (see Section 5.2).

6.2 Cluster mass estimate

Both our optical and X-ray data indicate that A523 is a massive cluster. Using the theoretical relation between mass and velocity dispersion of Munari et al. (2013, equation 1 checked on simulated clusters), the derived cluster mass is $M_{200,opt}(<R_{200,opt} = 1.9\ h_{70}^{-1}$ Mpc$) = 9.0 \times 10^{14}\ h_{70}^{-1}$ M$_{\odot}$, with related uncertainties of 8 per cent and 23 per cent on $R_{200,opt}$ and $M_{200,opt}$, as propagated from the error on σ_V. An additional 10 per cent of uncertainty on mass is indicated by the scatter around the theoretical relation which, however, does not take into account the cluster asphericity in the velocity ellipsoid (e.g. Wojtak 2013). From our measure of kT_{OUT} and the scaling relation of Arnaud et al. (2005), the derived cluster mass is $M_{200,X}(<R_{200,X} \sim 1.8\ h_{70}^{-1}$ Mpc$) \sim 7 \times 10^{14}\ h_{70}^{-1}$ M$_{\odot}$ in good agreement with the above optical estimate.

6.3 A merger scenario

According to the main optical and X-ray features (but see Section 6.5), A523 can be described as a binary head-on merger (BHOM) after the primary collision. In fact, it is characterized by two important galaxy subclusters and typical X-ray features noted in simulations (e.g. Ricker & Sarazin 2001; Poole et al. 2006). It also meets the typical BHOM selection criteria as listed by Mann & Ebeling (2011) that are the non-concentric X-ray contours and the large offset of the two BCGs from the X-ray peak.

The alignment of the directions defined by the two subclusters and by the elongation of X-ray isophotes indicates that SSW-NNE is the direction of the merging axis. The direction of the elongation of the large, diffuse BCG1 halo agrees, too. The small LOS velocity difference between the two subclusters indicates that the merger axis is almost perpendicular to the LOS or, alternatively, that the two subclusters are close to the turn around point. The first hypothesis is quite more reliable when analysing the merger kinematics with the use of the simple analytical bimodal model (e.g. Girardi et al. 2008 and references therein). According to our observational results, the relevant parameters of the two-body model are $V_{rf} = 100$–650 km s^{-1} for the relative LOS velocity, $D = 0.75\ h_{70}^{-1}$ Mpc for the projected distance, and $M_{system} = 0.7$–$0.9 \times 10^{14}\ h_{70}^{-1}$ M$_{\odot}$ for the mass of the system. A reliable assumption for the time relative to the core crossing is $t = 0.1$–0.3 Gyr since a few 10^8 years is the radiative lifetime of relativistic electrons losing energy. Moreover, comparable values have been found in previous studies of merging clusters hosting radio haloes, e.g. $t = 0.1$–0.2 Gyr is found in the case of the Bullet cluster (Markevitch et al. 2002), and $t = 0.2$–0.3 Gyr in Abell 520 (Girardi et al. 2008). Outgoing solutions are the only acceptable ones and α, the projection angle between the merging axis and the plane of the sky, is at most $\sim 10°$ in the $V_{rf} = 100$ km s^{-1} case and at most $\sim 30°$ in the $V_{rf} = 650$ km s^{-1} case. As for the mass ratio, both our spectroscopic and photometric optical data indicate that the southern cluster is comparable/slightly richer than the northern cluster, suggesting that the mass ratio is less than 2:1 (cf. the relative densities and galaxy contents in Tables 2 and 4).

Evidence of a merger in A523 provides additional support to the idea of a strong connection between the presence of a radio halo and an active dynamical status of the host cluster (see Section 1 and references therein). In particular, A523 also agrees with other halo radio clusters in the relations between the X-ray indicators of substructure, i.e. c versus w, w versus P_3/P_0, c versus P_3/P_0 (Cassano et al. 2010). Moreover, the BHOM scenario rules out the possibility that the radio source is a relic instead than a halo. In fact, in the outgoing shock-driven relic hypothesis we would expect that the subcluster, slowed down by gravitational effects, is preceded by the relic in its outgoing motion as shown by numerical simulations (e.g. Springel & Farrar 2007; Mastropietro & Burkert 2008), while the radio source in A523 is centred between the centres of the two subclusters.

6.4 Scaling relations

An interesting global cluster parameter is the value of the ratio between the energy per unit mass of galaxies to that of ICM as parametrized with $\beta_{spec} = \sigma_V^2/(kT/\mu m_p)$, where $\mu = 0.58$ is the mean molecular weight and m_p the proton mass. The value $\beta_{spec} = 1$ indicates the density–energy equipartition between ICM and galaxies. The mean β_{spec} value observed for massive clusters is consistent with unity both in nearby (Girardi et al. 1996, 1998) and in distant systems out to $z \sim 0.4$ (Mushotzky & Scharf 1997). Fig. 5 (bottom panel) shows how good is the agreement between X-ray temperature and velocity dispersion in the case of A523.

Numerical simulations show as both X-ray temperature and velocity dispersion rise due to the cluster merger, e.g. the temperature peaks either during the core-crossing or just after and then declines (Ricker & Sarazin 2001; Mastropietro & Burkert 2008), and similarly the velocity dispersion. However, a small enhancement of velocity dispersion is expected in the case of a merger axis perpendicular to the LOS (~ 20 per cent according to Pinkney et al. 1996) and A523 is indeed quite normal in the other relation involving global optical and X-ray properties. In fact, when considering our estimate of the bolometric X-ray luminosity
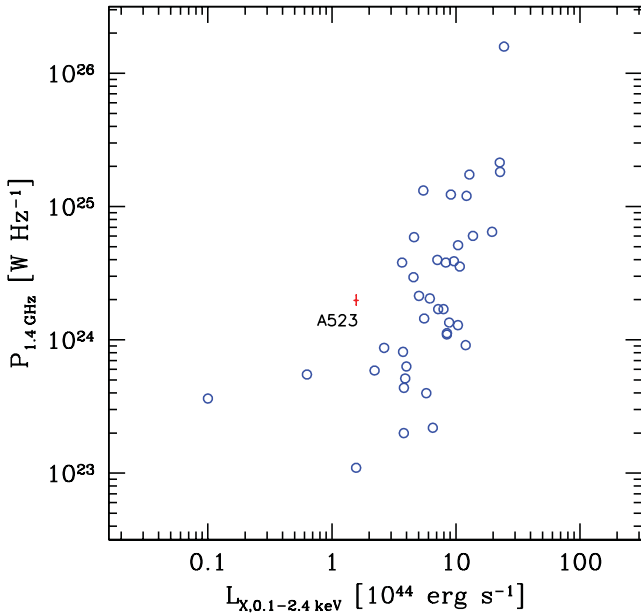
Figure 20. Total halo radio power at 1.4 GHz versus cluster X-ray luminosity in the 0.1–2.4 keV band. Blue circles refer to clusters plotted by Feretti et al. (2012). The position of A523 is indicated by the red cross and is based on our study.

($L_{X, \text{bol}, 500} = 3.44 \times 10^{44} \, h_{70}^{-2} \, \text{erg s}^{-1}$) and of the velocity dispersion ($\sigma_V = 950 \, \text{km s}^{-1}$), A523 lies very close to the L_X–σ relation as fitted by Zhang et al. (2011). Moreover, the A523 values are still acceptable in the L_X–T plane (as discussed in Section 4.4). We conclude that the agreement between σ_V and T quantities and their use as mass proxies are likely reliable.

As in the case of A523, most clusters showing radio haloes have a large gravitational mass, e.g. larger than $0.7 \times 10^{14} \, M_\odot$ within 2 Mpc (Giovannini & Feretti 2002; see also clusters analysed in our DARC program, Girardi et al. 2011 and references therein). In particular, when considering our estimate of the mass of A523 ($M_{500} \sim 5$–$6 \times 10^{14} \, h_{70}^{-1} \, M_\odot$, $M_{500} \sim 1/1.4 \times M_{200}$ for a typical NFW profile), this cluster is consistent with the relation between mass and radio power as traced for clusters hosting radio haloes (see fig. 3 of Cassano et al. 2013).

In spite of our revised upward X-ray luminosity, the peculiarity of A523 in the $P_{1.4\,\text{GHz}}$–L_X plane, already claimed by G11, is not solved and, rather, it should be considered more reliable due to the improvement of the data. In Fig. 20, A523 is compared to other $\sim$40 clusters as taken from Feretti et al. (2012). According to the relation fitted on $\sim$25 clusters by Cassano et al. (2013, see their fig. 2 and table 3), A523 is under luminous in X-ray by a factor of $\gtrsim$4 or over luminous in radio by a factor of $\gtrsim$24, which is inconsistent with the small uncertainties associated with the observational measures for A523 or with the scatter around the relation.

6.5 Suggestions for a more complex scenario

The peculiarity of A523 is not limited to the $P_{1.4\,\text{GHz}}$–L_X relation. Although our simulations in Section 5.2 show that a radio/X-ray peak offset can be explained in the context of a magnetic field energy on large spatial scales and suggest that peculiar halo elongations can be observed (see Fig. 19, middle and bottom left panels), it is still not obvious that we can explain a case like A523, where the halo

elongation is perpendicular to the merging axis as traced by X-ray and optical data.

Looking for a possible explanation of the A523 peculiarity, we note that, although earlier we discuss the A523 phenomenology in the framework of a BHOM scenario, it is known that distinguishing between binary and complex mergers is not easy (e.g. see the relevant discussion in Mann & Ebeling 2011). In the case of A523, both optical and radio data show some evidence in favour of a complex merger suggesting a scenario where A523 is forming at the cross of two filaments, along the SSW-NNE and ESE-WNW directions. From the X-ray side, a possible evidence in favour of a more complex dynamical status comes from the enhanced temperature in the northern region, more related to the radio halo position than the southern one.

In the context of a more complex scenario, the different main directions traced by radio and X-ray+optical data might refer to the two merging directions and, in particular, to be connected with the different time-scales intervening, with the radio halo better tracing the most recent accretion phenomena, although this accretion does not involve a lot of mass. Unfortunately, also due to the contamination of the background structure at $z \sim 0.14$, we need a larger redshift sample to probe the ESE-WNW direction of accretion. We also note that our current redshift catalogue samples only the cluster region within half R_{200}, making the cluster accretion phenomena only partially traced.

REFERENCES

Arnaud M., Pointecouteau E., Pratt G. W., 2005, A&A, 441, 893
Barrena R., Boschin W., Girardi M., Spolaor M., 2007, A&A, 467, 37
Barrena R., Girardi M., Boschin W., de Grandi S., Eckert D., Rossetti M., 2011, A&A, 529, A128
Bartalucci I., Mazzotta P., Bourdin H., Vikhlinin A., 2014, A&A, 566, A25
Beers T. C., Flynn K., Gebhardt K., 1990, AJ, 100, 32
Bird C. M., Beers T. C., 1993, AJ, 105, 1596
Böhringer H. et al., 2000, ApJS, 129, 435
Bonafede A. et al., 2009, A&A, 503, 707
Boschin W., Girardi M., Barrena R., Nonino M., 2012, A&A, 540, A43
Boschin W., Girardi M., Barrena R., 2013, MNRAS, 434, 772
Brown S., Rudnick L., 2009, AJ, 137, 3158
Brüggen M., van Weeren R. J., Röttgering H. J. A., 2011, Mem SAI, 82, 627

Brunetti G., Jones T. W., 2015, Magnetic Fields in Diffuse Media, Astrophysics and Space Science Library, Vol. 407, Springer-Verlag, Berlin, Heidelberg, p. 557

Brunetti G., Cassano R., Dolag K., Setti G., 2009, A&A, 507, 661

Buote D. A., 2002, in Feretti L., Gioia I. M., Giovannini G., eds, Merging Processes in Galaxy Clusters. Optical Analysis of Cluster Mergers. Kluwer Academic Publisher, the Netherlands

Buote D. A., Tsai J. C., 1996, ApJ, 458, 27

Cassano R., Ettori S., Giacintucci S., Brunetti G., Markevitch M., Venturi T., Gitti M., 2010, ApJ, 721, 82

Cassano R. et al., 2013, ApJ, 777, 141

den Hartog R., Katgert P., 1996, MNRAS, 279, 349

Dickey J. M., Lockman F. J., 1990, ARA&A, 28, 215

Dressler A., Shectman S. A., 1988, AJ, 95, 985

Ebeling H., Edge A. C., Böhringer H., Allen S. W., Crawford C. S., Fabian A. C., Voges W., Huchra J. P., 1998, MNRAS, 301, 881

Einasto M., Einasto J., Tago E., Müller V., Andernach H., 2001, AJ, 122, 2222

Enßlin T. A., Biermann P. L., Klein U., Kohle S., 1998, A&A, 332, 395

Fadda D., Girardi M., Giuricin G., Mardirossian F., Mezzetti M., 1996, ApJ, 473, 670

Feretti L., 1999, MPE Report No. 271, p. 3

Feretti L., 2005, in Sjouwerman L. O., Dyer K. K., eds, X-ray and Radio Connections. Published electronically by NRAO, http://www.aoc.nrao.edu/events/xraydio. Held 3–6 February 2004 in Santa Fe, New Mexico, USA

Feretti L., Gioia I. M., Giovannini G. eds., 2002, Astrophysics and Space Science Library, Vol. 272, Merging Processes in Galaxy Clusters. Kluwer Academic Publisher, the Netherlands

Feretti L., Bacchi M., Slee O. B., Giovannini G., Govoni F., Andernach H., Tsarevsky G., 2006, MNRAS, 368, 544

Feretti L., Giovannini G., Govoni F., Murgia M., 2012, Astron. Astrophys. Rev., 20, 54

Ferrari C., Govoni F., Schindler S., Bykov A. M., Rephaeli Y., 2008, Space Sci. Rev., 134, 93

Gal R. R., De Carvalho R. R., Brunner R., Odewahn S. C., Djorgovski S. G., 2000, AJ, 120, 540

Giovannini G., Feretti L., 2000, New Astron., 5, 335

Giovannini G., Feretti L., 2002, in Feretti L., Gioia I. M., Giovannini G., eds, Merging Processes in Galaxy Clusters. Diffuse Radio Sources and Cluster Mergers. Kluwer Academic Publisher, the Netherlands

Giovannini G., Feretti L., 2004, J. Korean Astron. Soc., 37, 323

Giovannini G., Feretti L., Girardi M., Govoni F., Murgia M., Vacca V., Bacchi J., 2011, A&A, 530, L5 (G11)

Girardi M., Biviano A., Giuricin G., Mardirossian F., Mezzetti M., 1993, ApJ, 404, 38

Girardi M., Fadda D., Giuricin G., Mardirossian F., Mezzetti M., Biviano A., 1996, ApJ, 457, 61

Girardi M., Escalera E., Fadda D., Giuricin G., Mardirossian M., Mezzetti M., 1997, ApJ, 482, 11

Girardi M., Giuricin G., Mardirossian F., Mezzetti M., Boschin W., 1998, ApJ, 505, 74

Girardi M., Barrena R., Boschin W., Ellingson E., 2008, A&A, 491, 379

Girardi M., Bardelli S., Barrena R., Boschin W., Gastaldello F., Nonino M., 2011, A&A, 536, A89

Govoni F., Enßlin T. A., Feretti L., Giovannini G., 2001a, A&A, 369, 441

Govoni F., Feretti L., Giovannini G., Böhringer H., Reiprich T. H., Murgia M., 2001b, A&A, 376, 803

Govoni F., Murgia M., Feretti L., Giovannini G., Dallacasa D., Taylor G. B., 2005, A&A, 430, L5

Govoni F., Murgia M., Feretti L., Giovannini G., Dolag K., Taylor G. B., 2006, A&A, 460, 425

Govoni F., Ferrari C., Feretti L., Vacca V., Murgia M., Giovannini G., Perley R., Benoist C., 2012, A&A, 545, A74

Kalberla P. M. W., Burton W. B., Hartmann D., Arnal E. M., Bajaja E., Morras R., Pöppel W. G. L., 2005, A&A, 440, 775 (LAB Map)

Kim K.-T., Kronberg P. P., Giovannini G., Venturi T., 1989, Nature, 341, 720

Leccardi A., Molendi S., 2008, A&A, 486, 359

Mann A. W., Ebeling H., 2011, MNRAS, 420, 2120

Markevitch M., Gonzalez A. H., David L., Vikhlinin A., Murray S., Forman W., Jones C., Tucker W., 2002, ApJ, 567, 27

Mastropietro C., Burkert A., 2008, MNRAS, 389, 967

Mohr J. J., Fabricant D. G., Geller M. J., 1993, ApJ, 413, 492

Munari E., Biviano A., Borgani S., Murante G., Fabjan D., 2013, MNRAS, 430, 2638

Murgia M., Govoni F., Feretti L., Giovannini G., Dallacasa D., Fanti R., Taylor G. B., Dolag K., 2004, A&A, 424, 429

Murgia M., Govoni F., Markevitch M., Feretti L., Giovannini G., Taylor G. B., Carretti E., 2009, A&A, 499, 679

Murgia M., Govoni F., Feretti L., Giovannini G., 2010, A&A, 509, A86

Mushotzky R. F., Scharf C. A., 1997, ApJ, 482, L13

Ogrean G. A., Brüggen M., van Weeren R. J., Röttgering H., Croston J. H., Hoeft M., 2013, MNRAS, 433, 812

Piffaretti R., Arnaud M., Pratt G. W., Pointecouteau E., Melin J.-B., 2011, A&A, 534, A109

Pinkney J., Roettiger K., Burns J. O., Bird C. M., 1996, ApJS, 104, 1

Pisani A., 1993, MNRAS, 265, 706 (1D-DEDICA)

Pisani A., 1996, MNRAS, 278, 697 (2D-DEDICA)

Pizzo R. F., de Bruyn A. G., Feretti L., Govoni F., 2008, A&A, 481, L91

Poole G. B., Fardal M. A., Babul A., McCarthy I. G., Quinn T., Wadsley J., 2006, MNRAS, 373, 881

Pratt G. W., Croston J. H., Arnaud M., Böhringer H., 2009, A&A, 498, 361

Ricker P. M., Sarazin C. L., 2001, ApJ, 561, 621

Rossetti M., Molendi S., 2010, A&A, 510, 83

Rossetti M., Eckert D., Cavalleri B. M., Molendi S., Gastaldello F., Ghizzardi S., 2011, A&A, 532, A123

Sanders J. S., 2006, MNRAS, 371, 829

Santos J. S., Rosati P., Tozzi P., Böhringer H., Ettori S., Bignamini A., 2008, A&A, 483, 35

Sarazin C. L., 2002, in Feretti L., Gioia I. M., Giovannini G., eds, Merging Processes in Galaxy Clusters. The Physics of Cluster Mergers. Kluwer Academic Publisher, the Netherlands

Schuecker P., Böhringer H., Reiprich T. H., Feretti L., 2001, A&A, 378, 408

Springel V., Farrar G. R., 2007, MNRAS, 380, 911

Tonry J., Davis M., 1979, ApJ, 84, 1511

Trimble P. C., 1993, MNRAS, 261, 57

Tukey J. W., 1960, in Olkin I., Ghurye S., Hoeffding W., Madow W., Mann H., eds, A Survey of Sampling from Contaminated Distributions. In Contributions to Probability and Statistics. Stanford University Press, Stanford, p. 448

Vacca V., Murgia M., Govoni F., Feretti L., Giovannini G., Orru E., Bonafede A., 2010, A&A, 514, A71

Vacca V., Govoni F., Murgia M., Giovannini G., Feretti L., Tugnoli M., Verheijen M. A., Taylor G. B., 2011, A&A, 535, A82

van Weeren R. J., Intema H. T., Oonk J. B. R., Röttgering H. J. A., Clarke T. E., 2009, A&A, 508, 1269

van Weeren R. J., Hoeft M., Röttgering H. J. A., Brüggen M., Intema H. T., van Velzen S., 2011a, A&A, 528, A38

van Weeren R. J., Brüggen M., Röttgering H. J. A., Hoeft M., Nuza S. E., Intema H. T., 2011b, A&A, 533, A35

Venturi T., 2011, Mem. SAIt, 82, 499

Wojtak R., 2013, A&A, 559, A89

Zhang Y.-Y., Andernach H., Caretta C. A., Reiprich T. H., Böhringer H., Puchwein E., Sijacki D., Girardi M., 2011, A&A, 526, A105

This paper has been typeset from a TeX/LaTeX file prepared by the author.